

Review

# Nano-Bismuth-Sulfide for Advanced Optoelectronics

Zimin Li<sup>1</sup> and Ye Tian<sup>2,3,\*</sup><sup>1</sup> Department of Network and New Media, Hunan City University, Yiyang 413000, China<sup>2</sup> School of Information and Electronic Engineering, Hunan City University, Yiyang 413000, China<sup>3</sup> Xi'an Micro Microelectronics Technology Institute, CASC, Xi'an 710054, China

\* Correspondence: tianye-man@163.com

**Abstract:** Bi<sub>2</sub>S<sub>3</sub> is a semiconductor with rational band gap around near-IR and visible range, and its nanostructures (or nano-Bi<sub>2</sub>S<sub>3</sub>) have attracted great attention due to its promising performances in optoelectronic materials and devices. An increasing number of reports point to the potential of such nanostructures to support a number of optical applications, such as photodetectors, solar cells and photocatalysts. With the aim of providing a comprehensive basis for exploiting the full potential of Bi<sub>2</sub>S<sub>3</sub> nanostructures on optoelectronics, we review the current progress in their controlled fabrication, the trends reported (from theoretical calculations and experimental observations) in their electrical properties and optical response, and their emerging applications.

**Keywords:** bismuth-sulfide; optoelectronics; nanostructure

## 1. Introduction

Chalcogenide materials are chemical compounds consisting of at least one chalcogen ion, i.e., a chemical element in column VI of the periodic table, also known as the oxygen family [1]. More precisely, the term chalcogenide refers to the sulphides (S), selenides (Se), and tellurides (Te). These compounds show similar patterns in their electron configuration (Figure 1), especially the outermost shells, resulting in similar trends in chemical behavior. On one hand, they are different from IV family elements such as silicon (Si) and germanium (Ge), serving as the “classic” semiconductors with tetrahedral coordinated lattices due to their strong covalent bonding. On the other hand, unlike the elements of the halogen family, with strong *sp*-hybridization for forming crystalline molecular structures, chalcogenide elements could form rich materials, including insulators, semiconductors as well as semimetals. These materials could be either molecular crystals or polymeric and layered crystals with distorted octahedral coordination. Such rich chemical and lattice structural features produce abundant electrical and optical properties. Accordingly, over the last decade, chalcogenide materials have attracted much attention, and intensive studies demonstrate their promising applications in phase change memory (PCM) [2], topological insulators [3], photo-catalysts [4], light-sources [5], etc.

Besides the unique properties of chalcogenide elements themselves, the chemical and physical behaviors of the chalcogenide materials also strongly depend on the elements to be chemically combined. Bismuth (Bi), as an outstanding *p*-block semimetal with a highly anisotropic Fermi surface [6], small effective electron mass, low carrier density, and long carrier mean-free path, can produce a strong relativistic effect [7]. Therefore the bismuth chalcogenide compounds, such as Bi<sub>2</sub>Se<sub>3</sub>, Bi<sub>2</sub>Te<sub>3</sub> and Bi<sub>2</sub>S<sub>3</sub>, have a number of notable chemical and physical properties [1,3,7], and have attained increasing significance for several fields, including quantum confinement [8], topological insulators [3], abnormal magnetoresistance [9], energy storage and conversion [10,11], thermoelectricity [12], etc. Hence, it is of value to review the current status of bismuth chalcogenide materials. In recent years, however, more attention has been paid to Bi<sub>2</sub>Se<sub>3</sub> and Bi<sub>2</sub>Te<sub>3</sub>, which are “star” materials, being well-known topological insulators [3], whereas the awareness of the



Citation: Li, Z.; Tian, Y.

Nano-Bismuth-Sulfide for Advanced Optoelectronics. *Photonics* **2022**, *9*, 790. <https://doi.org/10.3390/photonics9110790>

Received: 31 August 2022

Accepted: 18 October 2022

Published: 24 October 2022

**Publisher's Note:** MDPI stays neutral with regard to jurisdictional claims in published maps and institutional affiliations.



**Copyright:** © 2022 by the authors. Licensee MDPI, Basel, Switzerland. This article is an open access article distributed under the terms and conditions of the Creative Commons Attribution (CC BY) license (<https://creativecommons.org/licenses/by/4.0/>).

advances on  $\text{Bi}_2\text{S}_3$  materials is relatively sparse. However, as a *n*-type semiconductor with relative low symmetric space group [13],  $\text{Bi}_2\text{S}_3$  shows great potential in solar cells [14], hydrogen storage [15], photo-catalysts [16], optical-detection [17], memristors [18,19], etc. Moreover, in these applications, constructing nanostructures with rich surface sites seems of great significance, thanks to their strong nano-size effect [13,18,20–22]. Therefore, it is valuable to review the research progress on nano-bismuth-sulfide. In this paper, we review recent advances in bismuth-sulfide nanostructures for optoelectronics to track the rapid development in this field, highlight the most recent scientific discoveries, and predict future trends for nano-bismuth-sulfide as well as its applications.

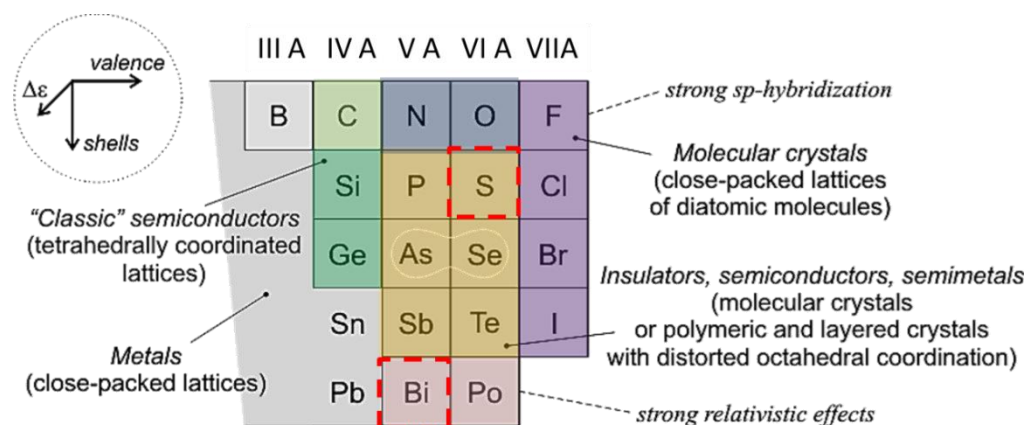


**Figure 1.** Unique electron configurations of both the bismuth and chalcogenide systems.

The remainder of this paper is organized as follows: Section 2 discusses various fabrication methods of nano- $\text{Bi}_2\text{S}_3$ ; Section 3 describes the basic electronic and optical properties of  $\text{Bi}_2\text{S}_3$ ; Section 4 focuses on the emerging optoelectronic applications. Finally, conclusions and perspectives are drawn in Section 5.

## 2. Fabrications

Amount of  $\text{Bi}_2\text{S}_3$  nanostructures were successfully prepared, namely 0D nanostructures (e.g., nanoparticles and nanospheres), 1D nanostructures (including nanowires and nanorods), and 2D nanostructures (including nanoplates, nanosheets, and thin films), with continuously improved crystalline quality [13,16–18,23–47]. The sizes of these structures range from a few atoms to a few microns, which makes them broadly suitable for studies in various fields, including hydrogen storage [48], thermoelectricity [46], memristors [21], photocatalysts [49], solar cells [26], and photodetection [50]. It is doubtless that the broad size range of the existing  $\text{Bi}_2\text{S}_3$  nanostructures could provide abundant building blocks for constructing optical responsible systems.

Actually, over the past few years, the fabrication methods of  $\text{Bi}_2\text{S}_3$  nanostructures were explored intensively (see Table 1). Physical or chemical deposition and direct solvothermal synthesis are commonly employed, while some other methods, including chemical precipitation, reflux, sol-gel method, hot-injection, and high power sonication process have also been reported [4,16,32,51,52]. These methods can produce 0D nanoparticles, 1D nanorods, and nanoribbon, as well as 2D nano-thin film. The solution-phase synthesis is the most frequently employed method utilized to prepare various  $\text{Bi}_2\text{S}_3$  nanostructures [23,27,28] while physical vapor depositions (PVD, including magnetron sputter thermal evaporation and pulse laser deposition) have demonstrated their value in the photovoltaic field for electron-transport layers (ETL) and light-absorption layers [14,26]. Especially for hybrid perovskite solar cells, when potential contamination and variations introduced by the solvents are undesired, thermal evaporation is proposed as a rational route for preparing  $\text{Bi}_2\text{S}_3$  nano-thin film as the ETL without introducing any solvents [26]. Generally, the fabrication methods of the nano- $\text{Bi}_2\text{S}_3$  can be cataloged as two types: “top-down” and “bottom up”. It is quite straightforward that several vapor or liquid phase-deposition methods belong to

the “top-down” family, and direct surface sulfurization is also an alternative “top-down” approach, while solvothermal synthesis is the most popular “bottom up” method. In the following, these two kinds of methods are discussed sequentially.

Vapor phase deposition (VPD) is one of most frequently used methods for nanofabrication, with the potential for mass production [7]. It has achieved great successes in various field, including integrated circuits [53], semiconductor lasers [54], bio-sensing [55], etc. For the preparation of nano-Bi<sub>2</sub>S<sub>3</sub>, especially thin film, VPD, such as thermal evaporation (Figure 2a), pulse laser deposition (PLD), and low-pressure metal–organic chemical vapor deposition (LP-MOCVD) could be feasible tools [14,26,56]. Moreover, while regularly employed in light-absorption layers [56], VPD-fabricated nano-Bi<sub>2</sub>S<sub>3</sub> also exhibits unique value as high performance inorganic electron transport layers for perovskite solar cells to avoid contamination and variations introduced by the solvent process [26], as well as serving as energy conversion media for quantum dot-sensitized solar cells (QDSSCs) [14]. In addition to the VPD methods, Bi<sub>2</sub>S<sub>3</sub> thin film can also be prepared by chemical bath or electrochemical deposition [33,57]. These deposition routes may introduce impurity or contamination, but could be more cost-effective (Figure 2b). Moreover, using a vapor-phase sulfur source to sulfurize the bismuth-based metal-organic framework or bismuth oxide could achieve “top-down” Bi<sub>2</sub>S<sub>3</sub> nanostructures (Figure 2c–e) [29]. These surface sulfurization routes need high temperature, but could provide better crystalline quality.

Aside from the “top-down” deposition, “bottom-up” solvothermal synthesis seems more popular for the fabrication of various Bi<sub>2</sub>S<sub>3</sub> samples with a high level of control in their shapes, such as 0D, 1D, and 2D nanostructures [17,28,30,34,58,59]. As the liquid-phase progresses, it employs the bismuth source and sulfur source to react in solution. Bi(NO<sub>3</sub>)<sub>3</sub> is the most popular bismuth source, but some other choices, such as BiCl<sub>3</sub> and BiOX (X = Cl, Br, I) are also available [11,33,60,61], while the sulfur source could be either organic (TAA, KSCN, etc.) or inorganic (Na<sub>2</sub>S, Na<sub>2</sub>S<sub>2</sub>O<sub>3</sub>). The reaction temperatures are usually moderate (<200 °C), and the synthesis duration varies from a few minutes to a few days [39,58]. The most typical product of the solvothermal synthesis is the 1D rod or wire (Figure 2f). The diameter of the nanorod or nanowire is <100 nm, while the length could be facile to tens μm. Such 1D growth often tends to extend along the [001] direction, with a corresponding length-to-diameter ratio greater than 10 [22]. When the hydrothermal synthesis is assisted with glucose, hollow nanotubes can also be produced by 1D growth [60]. In addition, nanoribbon can also be solvothermally synthesized, and interestingly, the process is rather fast (a few minutes), possibly representing an highly efficient route to mass production [58]. Moreover, in some other cases, due to the change in the sulfur source, the morphology could transform from nanowire to nanoparticles, wire bundles, urchin-like nano-/microspheres, or microspheres with cavities, as well as chrysanthemum-like Bi<sub>2</sub>S<sub>3</sub> nanostructures [59].

**Table 1.** Selected reports on “top-down” and “bottom-up” fabrication of the nano-Bi<sub>2</sub>S<sub>3</sub>.

Method	Growth Condition	Starting Materials	Product	Size
<b>“Top-down” fabrications</b>				
<b>Vapor phase deposition</b>				
Thermal evaporation [26]	RT	Bi <sub>2</sub> S <sub>3</sub> power	Amorphous film	50 nm thickness
LP-MOCVD [56]	450 °C	[Bi(S <sub>2</sub> CNMen-Hex) <sub>3</sub> ] [Cd(S <sub>2</sub> CNMen-Hex) <sub>2</sub> ]	Fiber-like particles	Length (L): 1 μm diameter (D): 50 nm
Pulsed laser deposition [14]	RT	Bi <sub>2</sub> S <sub>3</sub> target	Quantum dots	D < 5 nm
<b>Liquid phase deposition</b>				
Cathodic electrodeposition [41]	RT	Na <sub>2</sub> S <sub>2</sub> O <sub>3</sub> , Na <sub>3</sub> C <sub>6</sub> H <sub>5</sub> O <sub>7</sub> Bi(NO <sub>3</sub> ) <sub>3</sub> ,	Thin film	/
Electrodeposition [62]	RT	Na <sub>2</sub> S <sub>2</sub> O <sub>3</sub> , Bi(NO <sub>3</sub> ) <sub>3</sub> , EDTA	Thin film	/
Chemical bath deposition(CBD) [33]	RT	Bi(NO <sub>3</sub> ) <sub>3</sub> , thioacetamide (TA), ammonium citrate (AC)	Nanowall Bi <sub>2</sub> S <sub>3</sub> films	/

**Table 1.** Cont.

Method	Growth Condition	Starting Materials	Product	Size
CBD [26]	RT	Bi(NO <sub>3</sub> ) <sub>3</sub> , triethanolamine (TEA), TA,	Thin film	Thickness (T): 50–140 nm
Non-aqueous CBD [63]	RT	Bi(NO <sub>3</sub> ) <sub>3</sub> , acetic acid, TA	Thin films	T: 241 nm
Non-aqueous CBD [42]	RT	Bi(NO <sub>3</sub> ) <sub>3</sub> , Na <sub>2</sub> S <sub>2</sub> O <sub>3</sub> , formaldehyde,	Thin film	T: 50–100 nm
<b>Surface Sulfurization</b>				
High-temperature reaction of sulfur source with bismuth-based metal–organic framework [64]	300~600 °C	Bi(BTC)(DMF)·DMF·(CH <sub>3</sub> OH) <sub>2</sub> Trimesic acid (H <sub>3</sub> BTC)	Nanorod (NR)	D: 60 nm
Surface sulfurization [29]	450 °C	Bi <sub>2</sub> O <sub>3</sub> Nanosheets	2D nanosheets	T: 2.5 nm
<b>“Bottom-up” fabrications</b>				
<b>Solvothermal synthesis</b>				
Hydrothermal synthesis [30]	160 °C	Bi(NO <sub>3</sub> ) <sub>3</sub> , NH <sub>2</sub> CSNH <sub>2</sub> , thiourea	NR	D: 50~100 nm L: 1~2 μm
Hydrothermal process [11]	180 °C	BiCl <sub>3</sub> , HCl, TAA	Bi <sub>2</sub> S <sub>3</sub> nanomeshes	L: 200 nm D: 20~40 nm
Hydrothermal process [65]	180 °C	Bi(NO <sub>3</sub> ) <sub>3</sub> , Thiourea, Urea, Methyl orange	Microsphere	D: 3 μm
Hydrothermal methods [59]	180 °C	Bi(NO <sub>3</sub> ) <sub>3</sub> , thiourea (TU), potassium thiocyanate (KSCN), TAA, sodium thiosulfate (Na <sub>2</sub> S <sub>2</sub> O <sub>3</sub> ·5H <sub>2</sub> O)	Nanowires (NW), wire bundles, urchin-like nano-/microspheres microspheres with cavities	NW D: 15~40 nm L: Tens μm bundles D: 2~3 μm L: 13~20 μm sphere D: ~1 μm/
Solvothermal synthesis [66]	160 °C	Bi(NO <sub>3</sub> ) <sub>3</sub> , ethylene glycol (EG), TAA, TU, L-cysteine	Nanoparticles, urchin-like spheres	/
solvothermal method [67]	80 °C	Bi(NO <sub>3</sub> ) <sub>3</sub> , EG, TU, poly(vinylpyrrolidone) (K-30)	Chrysanthemum-like nano-Bi <sub>2</sub> S <sub>3</sub>	D: ~500 nm.
Solvothermal method [58]	150 °C 5 min	Oleyl amine, sulfur powder, BiCl <sub>3</sub> , oleic acid, hexane, 1-octadecene	Nanoribbons	D: 10~80 nm L: 100~500 nm
Hydrothermal route [68]	160 °C	Bi(NO <sub>3</sub> ) <sub>3</sub> , TAA, DA, ascorbic acid (AA), uric acid (UA), paracetamol	NR	L: 100 nm
Hydrothermal method [60]	180 °C	Bi(NO <sub>3</sub> ) <sub>3</sub> , Na <sub>2</sub> S <sub>2</sub> O <sub>3</sub> , glucose	Hollow nanotubes	L: dozens μm D: few μm
Hydrothermal method [43]	180 °C 2 days	Bi(NO <sub>3</sub> ) <sub>3</sub> , Na <sub>2</sub> S <sub>2</sub> O <sub>3</sub> ,	NW	D: 20–60 nm
Hydrothermal method [39]	180 °C 3 day	Tetramethylammonium Bi(NO <sub>3</sub> ) <sub>3</sub> , hydroxide, Na <sub>2</sub> S	NW	D: 60 nm
Wet chemical synthesis [69]	150 °C/1 h and then 240 °C/2 h	Bi(NO <sub>3</sub> ) <sub>3</sub> , methanol, hydrochloric acid, thiourea	NR	D: 20–40 nm L: 200–600 nm
<b>Other methods</b>				
Chemical precipitation [32]	70 °C	Bi(NO <sub>3</sub> ) <sub>3</sub> , Thioacetamide (C <sub>2</sub> H <sub>5</sub> NS), HCl	Nanoparticle	D: 10–50 nm
Reflux [16]	140 °C	Bi(NO <sub>3</sub> ) <sub>3</sub> , citric acid, TU, CTAB DMF, EG, PEG	NR, nanoparticle	D < 40 nm
Sol-gel method [51,52]	180 °C	Bi(NO <sub>3</sub> ) <sub>3</sub> , TU, polyvinyl pyrrolidone, lithium hydroxide, EG	NR	D: 200 nm
Hot-injection [4]	180 °C	Bismuth chloride thioacetamide	NR	D: 7~20 nm, L: 30~70 nm
High power sonication process [24]	RT	Bi <sub>2</sub> S <sub>3</sub> powder	Nanoribbons	L: ~10 μm Width (W): ~40 nm

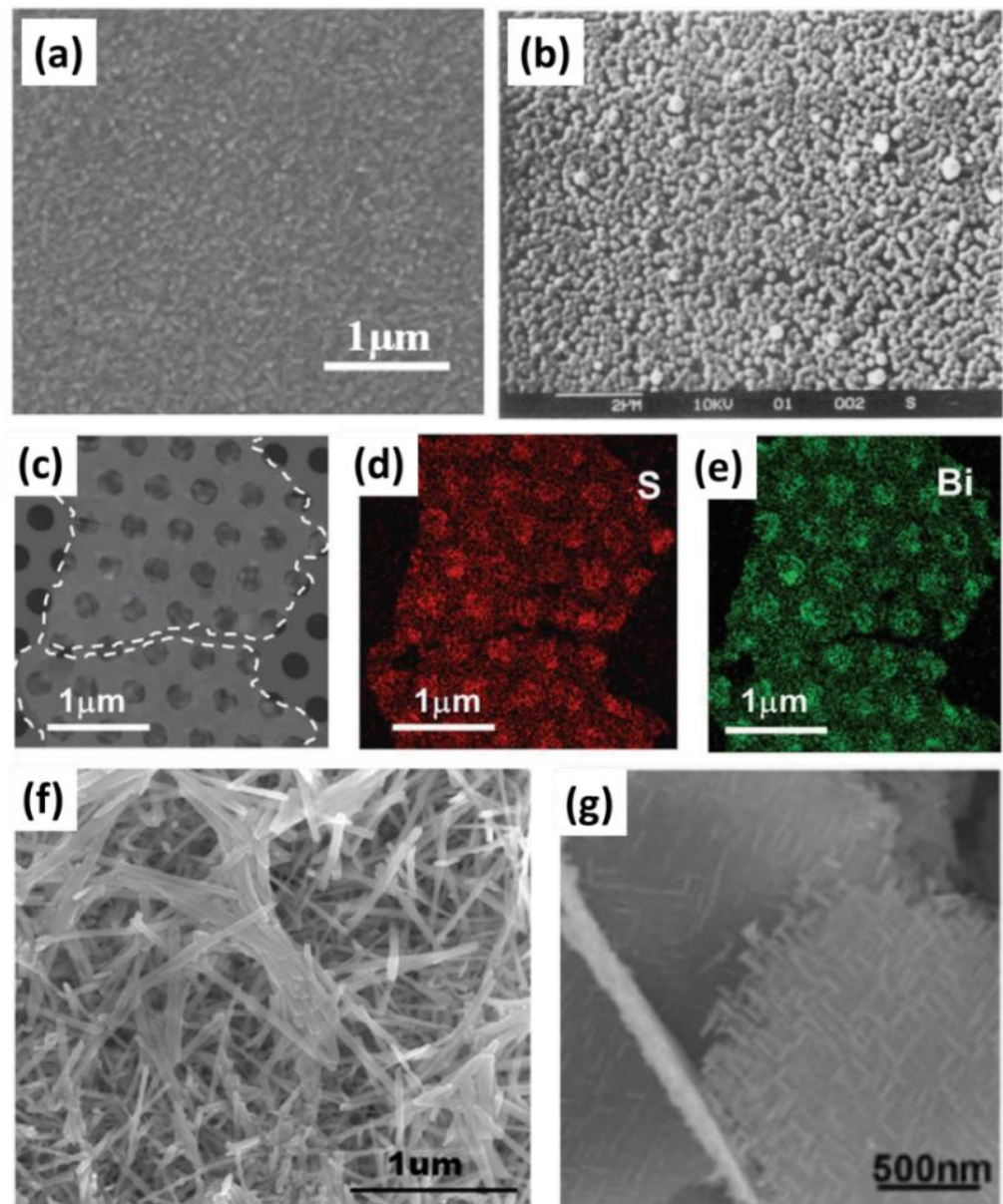


**Figure 2.** SEM of (a)  $\text{Bi}_2\text{S}_3$  thin film prepared by thermal evaporation (reprinted with permission from [70] © 2022, Elsevier), (b)  $\text{Bi}_2\text{S}_3$  thin film prepared by CBD (reprinted with permission from [42] © 2022, Elsevier). TEM image of (c)  $\text{Bi}_2\text{S}_3$  nanosheet, as well as its (d) S-element and (e) Bi-element mapping (reprinted with permission from [29] © 2022, Wiley-VCH); SEM image of (f)  $\text{Bi}_2\text{S}_3$  nanowire prepared by solvothermal synthesis (reprinted with permission from [43] © 2022, Elsevier) and (g)  $\text{BiOCl-Bi}_2\text{S}_3$  hierarchical nanosheet (reprinted with permission from [28] © 2022, Wiley-VCH).

Besides the pure  $\text{Bi}_2\text{S}_3$  nanostructures, there are also several hierarchical and/or heterogeneous structures based on nano- $\text{Bi}_2\text{S}_3$  (Table 2), and they are fabricated (usually) through the combination of “top-down” and “bottom-up” routes [49,51,52,71–74] (Figure 2g). Thanks to the high surface-to-volume ratio of such nano- $\text{Bi}_2\text{S}_3$ -based hierarchical and/or heterogeneous structures, they are quite promising for applications such as Li- or Na- ion battery, photocatalysts, and so on [10,52,73,75].

**Table 2.** Selected reports on the fabrication of Bi<sub>2</sub>S<sub>3</sub>-based hierarchical and heterogeneous microstructures.

Method	Growth Condition	Start Materials	Product	Size
Topotactical transformation [72]	180 °C	Bi(NO <sub>3</sub> ) <sub>3</sub> , TU	Bi <sub>2</sub> S <sub>3</sub> /Bi <sub>2</sub> WO <sub>6</sub> hierarchical microstructures	D: ~2 μm
Topotactical transformation [76]	80 °C	BiOCl, TAA	Bi <sub>2</sub> S <sub>3</sub> hierarchical microstructures	D: 30~200 nm
In situ ion-exchange process [73]	120 °C	BiCl <sub>3</sub> , ethanol.	Bi <sub>2</sub> S <sub>3</sub> /ZnS microspheres	D: 200~500 nm
Solvothermal method [77]	160 °C	Bi(NO <sub>3</sub> ) <sub>3</sub> , glycol, L-lysine, CuCl <sub>2</sub>	CuS–Bi <sub>2</sub> S <sub>3</sub> microspheres and cockscomb-like structures	D: 500–5 μm
Hydrothermal route [10]	180 °C	Thioacetamide, ethanol, glycerol, BiCl <sub>3</sub>	Nanostructured Bi <sub>2</sub> S <sub>3</sub> encapsulated within 3D N-doped graphene	500–2000 nm

### 3. Optoelectronic Properties of Nano-Bismuth-Sulfide

#### 3.1. Electronic Band Structure and Conduction Properties

Bi<sub>2</sub>S<sub>3</sub> has an orthorhombic crystal structure ( $a = 11.305 \text{ \AA}$ ,  $b = 3.981 \text{ \AA}$ ,  $c = 11.147 \text{ \AA}$ ) with the space group  $pbnm$  (62) [13]. It has four molecules per unit cell [18,19], and each molecule contains two bismuth atoms and three sulfide atoms, which add up to 20 atoms per unit cell (Figure 3a). The relatively low symmetry of the space group implies that the crystal structure of Bi<sub>2</sub>S<sub>3</sub> consists of five non-equivalent atoms: two non-equivalent Bi sites and three non-equivalent S sites [13]. It has a special layered structure and weak bonds between the layered units, which leads to the anisotropy of Bi<sub>2</sub>S<sub>3</sub> growth [24]. Its band gap is 1.3~1.7 eV at room temperature (RT), and the first principle calculated value is 1.335 eV using a local density approach, as shown in Figure 3b [19]. However, if spin-orbit coupling (SOC) is considered, the band gap would decrease to ~1.2 eV [13]. These experimental and theoretical results indicate that Bi<sub>2</sub>S<sub>3</sub> could produce a large absorption coefficient around the near-infrared and visual range [17,19,78]. Moreover, Bi<sub>2</sub>S<sub>3</sub> is intrinsically *n*-type, with a carrier concentration of  $n = 3 \times 10^{18} \text{ cm}^{-3}$  at RT, and its RT electron mobility is  $\mu_n = 200 \text{ cm}^2/\text{Vs}$  [26]. Accordingly, the intrinsic RT resistivity of Bi<sub>2</sub>S<sub>3</sub> is  $\sim 10^5 \text{ \Omega cm}$ . Furthermore, the electrical conduction of Bi<sub>2</sub>S<sub>3</sub> is temperature dependent due to its semiconduction nature, and highly anisotropic due to its low crystalline symmetry [79]. It can exhibit temperature-dependent conduction activation behavior, and potentially unique thermoelectric behavior, which could be used for thermal power devices [12,80]. It also has several other interesting electrical properties, including the Meyer–Neldel rule (MNR), resistive switching, etc. [18,19,81].

For the thermal power feature of Bi<sub>2</sub>S<sub>3</sub>, the typical Seebeck coefficient of Bi<sub>2</sub>S<sub>3</sub> could be higher than  $400 \text{ \mu V K}^{-1}$ , and its figure of merit (ZT value) could reach 0.72 at 773 K with rational CuBr<sub>2</sub> doping (Figure 4a–d), and even the average ZT value over the temperature from 300 K to 773 K, for more accurate evaluation of the thermoelectric efficiency, is still up to 0.40 (see Figure 4e) [82]. These promising reports make Bi<sub>2</sub>S<sub>3</sub>, Bi<sub>2</sub>Se<sub>3</sub>, and Bi<sub>2</sub>Te<sub>3</sub> a potential material family for heat-energy conversion [12,46,83]. Moreover, nano-structured bulk samples of Bi<sub>2</sub>S<sub>3</sub> made from surface-treated Bi<sub>2</sub>S<sub>3</sub> nanonetworks present ZT of 0.5 at 723 K [76], thanks to its improved electrical conductivity and low thermal conductivity compared with samples made from solution-synthesized materials or ball-milled powders. Moreover, as nano-scale Bi<sub>2</sub>S<sub>3</sub> precipitates, it seems beneficial to improve the thermoelectric property of Cu<sub>x</sub>Bi<sub>2</sub>SeS<sub>2</sub> [28]. Some selected reports about Bi<sub>2</sub>S<sub>3</sub>-based the thermal power device are listed in Table 3.

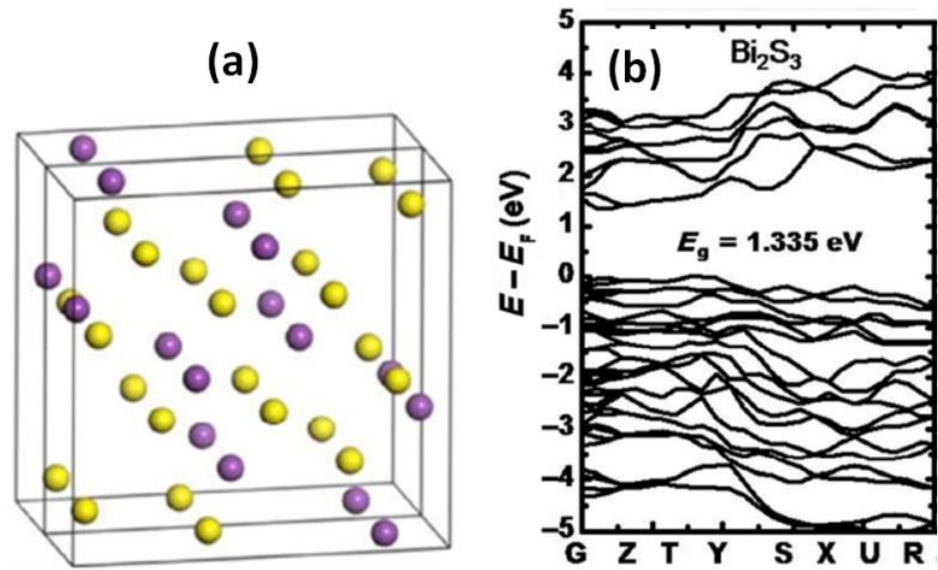


**Figure 3.** (a) Crystalline model of  $\text{Bi}_2\text{S}_3$  and (b) its band structure calculated by first-principle simulation. (Reprinted with permission from [21] © 2022, Springer Nature).

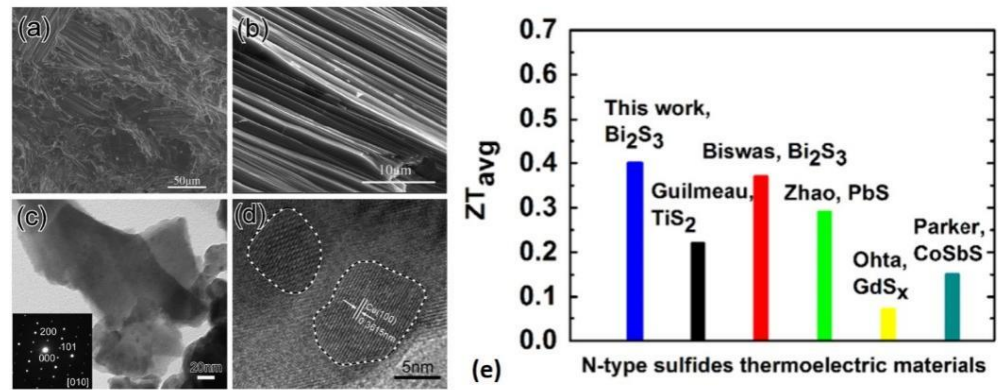


**Figure 4.**  $\text{Bi}_2\text{S}_3$  with rational  $\text{CuBr}_2$  doping: (a) scanning electron microscopy (SEM) of  $\text{CuBr}_2$ -doped  $\text{Bi}_2\text{S}_3$  and (b) its high amplified imaging to sample details; (c) transmission electron microscopy (TEM) of  $\text{CuBr}_2$ -doped  $\text{Bi}_2\text{S}_3$  and its selective area electron diffraction (SAED); (d) high-resolution TEM for lattice nature of the sample; (e) ZT value comparison between  $\text{CuBr}_2$ -doped  $\text{Bi}_2\text{S}_3$  and other  $\text{Bi}_2\text{S}_3$ -based thermal power systems. (Reprinted with permission from [82] © 2022, Elsevier).

**Table 3.** Selected reports about the  $\text{Bi}_2\text{S}_3$ -based thermal power device.

Sample	Electrical Conductivity (S/cm)	Thermal Conductivity ( $\text{W}\cdot\text{m}^{-1}\cdot\text{K}^{-1}$ )	Seebeck Coefficient ( $\mu\text{V}/\text{K}$ )	Power Factor ( $\mu\text{W}\cdot\text{cm}^{-1}\cdot\text{K}^{-2}$ )	ZT Value
$\text{Bi}_2\text{S}_3$ powder [12]	7.153@628 K	0.54~0.75	390~440	~1.15@628 K	~0.11@628 K
$\text{Bi}_2\text{S}_3$ @Ni powder [12]	28.9~38.4	0.4~0.48	180~291	2.44@628 K	0.38@628 K
Pristine $\text{Bi}_2\text{S}_3$ [80]	2.6	0.45~0.85	455@673 K	~1.6	~0.15@773 K
I-doping $\text{Bi}_2\text{S}_3$ [80]	~30	0.42~0.82	375@773 K	3.1	0.58@773 K
$\text{Bi}_2\text{S}_3$ nanobeads [84]	~160@RT	/	~65	/	/
$\text{Bi}_2\text{S}_3$ nanoparticles [32]	/	/	315~375	/	/

Table 3. Cont.

Sample	Electrical Conductivity (S/cm)	Thermal Conductivity (W·m <sup>-1</sup> ·K <sup>-1</sup> )	Seebeck Coefficient (μV/K)	Power Factor (μW·cm <sup>-1</sup> ·K <sup>-2</sup> )	ZT Value
CuBr2 doping Bi <sub>2</sub> S <sub>3</sub> [82]	2.2	1.3	418.5	1.	~0.1@773 K
	187.6	1.0	155.9	/	~0.4@773 K
	309.6	1.0	113.9	/	0.72@773 K
	225.2	0.7	114.6	/	~0.5@773 K
Se and Cl doping Bi <sub>2</sub> S <sub>3</sub> [35]	/	/	/	2.0	~0.6@723 K
Surface-treated Bi <sub>2</sub> S <sub>3</sub> nanonetwork [76]	333	/	56.8	/	0.5@723 K

As for the thermal activation of the conduction, MNR has been found in a wide variety of thermally activated processes [13,81]. Basically, MNR is ascribed to the disorder [48], which could introduce a (large) density of localized states (traps) in material, and accordingly the  $E_{MN}$  of the material is deemed as a measure of its disorder. MNR states generate in a thermally activated process, such as the temperature-dependence of the resistivity ( $\rho$ ) of semiconductors [18]

$$\rho = -\rho_0 \exp (E_a/kT) \tag{1}$$

The increase in activation energy  $E_a$  is partially compensated by the increase in prefactor ( $\rho_0$ ) [18]:

$$\ln\rho_0 = \ln\rho_{00} + E_a/E_{MN} \tag{2}$$

where  $E_{MN}$  is “Meyer–Neldel” energy, and  $\rho_{00}$  is the “intrinsic” resistivity related to the material itself. In Bi<sub>2</sub>S<sub>3</sub> systems, MNR reveals several carrier-trapping-related transport behaviors [13,81]. In Bi<sub>2</sub>S<sub>3</sub> nested nanonetworks (BSNNN, Figure 5a), normal MNR is observed with  $E_{MN}$  as 43 meV, as shown in Figure 5b [81]. This is in line with the studies of single Bi<sub>2</sub>S<sub>3</sub> nanowires, where  $E_{MN}$  is 38 meV (see Figure 5c,d) [13,48]. However, the annealing treatment of the samples could change the positive  $E_{MN}$  to negative (Figure 5e) [13,48]. Different MNR behaviors can be understood under the unified framework based on the trap-limited-current-based model of MNR, which could naturally produce either positive or negative  $E_{MN}$  [48].

Moreover, Bi<sub>2</sub>S<sub>3</sub> could also be resistively switchable. Specifically, the conductance of the interfaces of Pt/Bi<sub>2</sub>S<sub>3</sub> and FTO/Bi<sub>2</sub>S<sub>3</sub> can be bipolar switched [57]. Such bipolar switching can be highly continuous, and seems quite promising for application in memristors for neural computing, thanks to its good bivariate-continuous-tunable memristance, as shown in Figure 6 [21]. The atomic origin of such memristive features is the carrier-trapping at the interface induced by oxygen-doping [19], which is revealed by combining  $I$ - $V$  characterization (Figure 6b,c), electron energy-loss spectroscopy (EELS, Figure 7a–d), and first-principle calculation (Figure 7e).

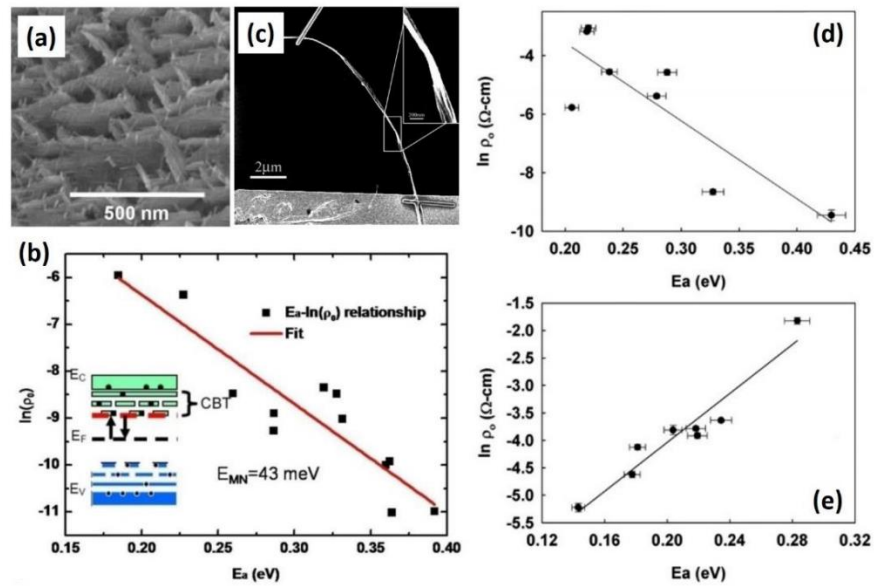


**Figure 5.** (a) SEM of  $\text{Bi}_2\text{S}_3$  nested nano-networks; (b) MNR behavior of  $\text{Bi}_2\text{S}_3$  nested nanonetworks (reprinted with permission from [18] © 2022, Springer Nature); (c) SEM of  $\text{Bi}_2\text{S}_3$  nanowire; (d) MNR behavior of  $\text{Bi}_2\text{S}_3$  nanowire; (e) anti-MNR behavior of  $\text{Bi}_2\text{S}_3$  nanowire after annealing. Reprinted with permission from April Dawn Schricker, “Electrical Properties of Single GaAs,  $\text{Bi}_2\text{S}_3$  and Ge Nanowires” (2005), Dissertation.

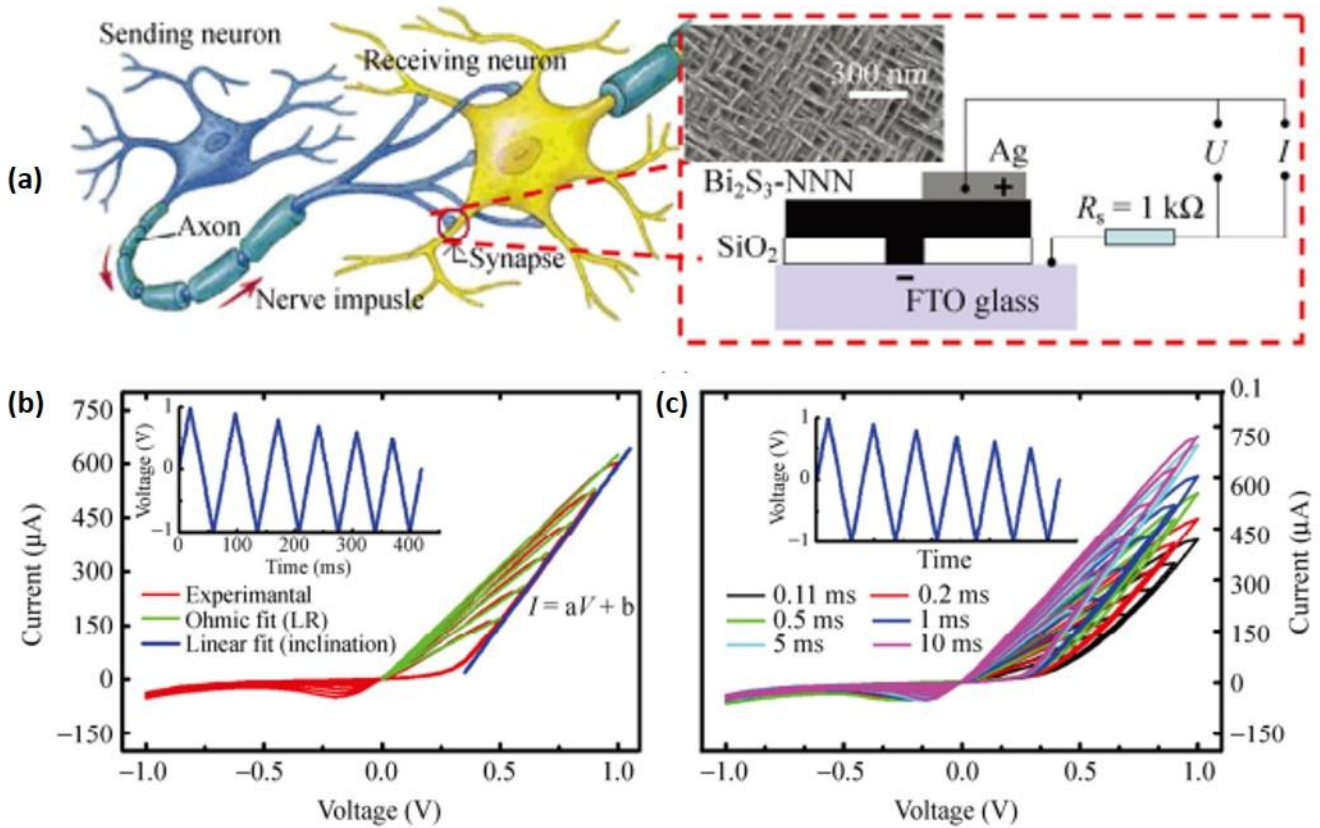


**Figure 6.** (a) Scheme of FTO/ $\text{Bi}_2\text{S}_3$ -based memristor for neural emulation; bivariate-continuous tunable memristance of FTO/ $\text{Bi}_2\text{S}_3$  with both (b) voltage strength and (c) stimulus duration tunability. (Reprinted with permission from [21] © 2022, Springer Nature).

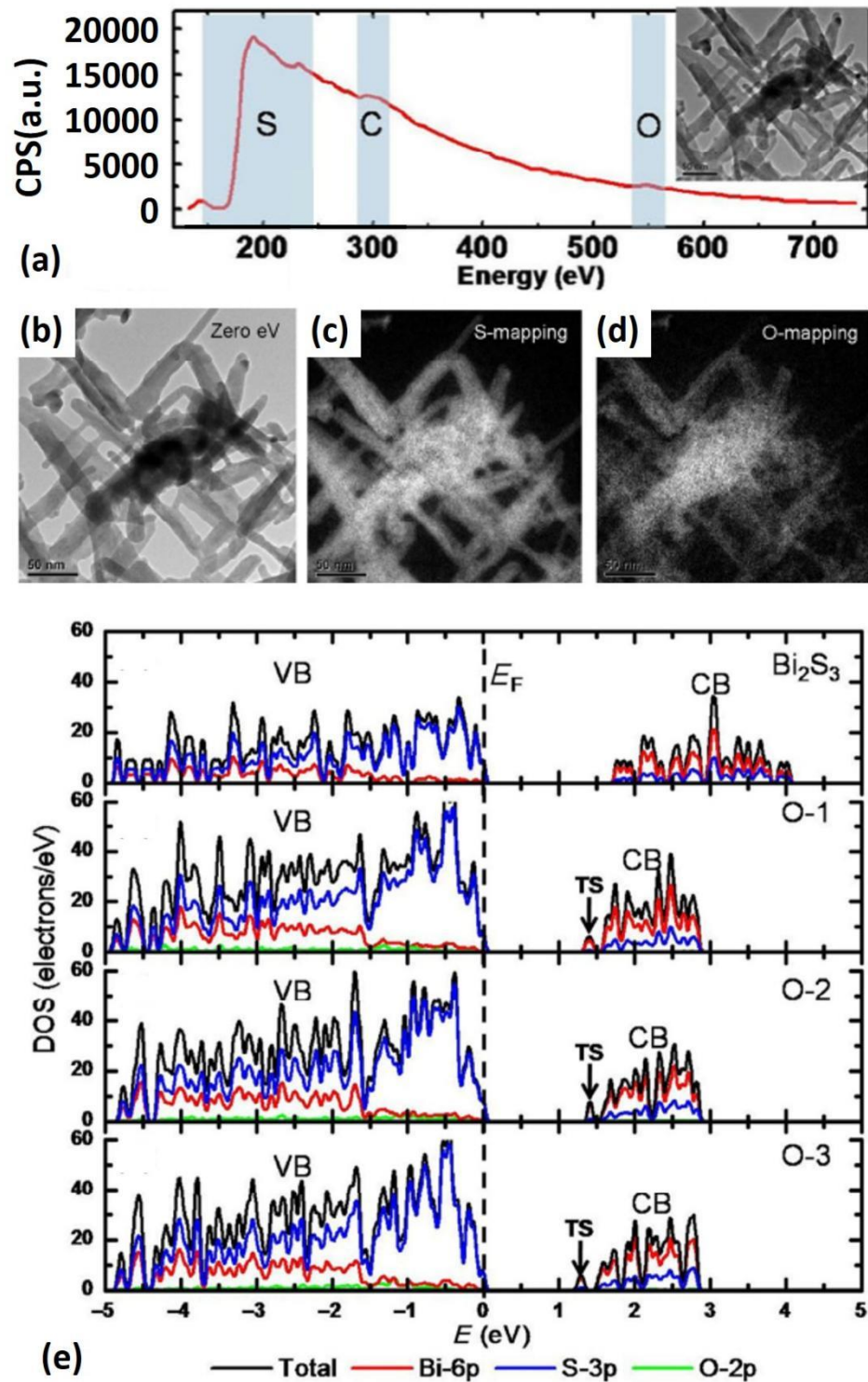


**Figure 7.** (a) EELS of BSNNN and its energy-loss filtering imaging and/or element mapping at (b) Zero-eV, (c) S-peak, and (d) O-peak. (e) Density of state (DOS) of Bi<sub>2</sub>S<sub>3</sub> and Bi<sub>2</sub>S<sub>3</sub> with different O-doping site predicted by first-principal calculation. (VB: valence band; CB: conduction band; TS: trap state; reprinted with permission from [21] © 2022, Springer Nature).

### 3.2. Optical Properties

As proposed in Section 3.1, the bandgap of (bulk) Bi<sub>2</sub>S<sub>3</sub> is ~1.3 eV, hence could produce a large absorption coefficient around near-infrared and visual range. Especially for applications such as solar energy, the high absorption coefficient of Bi<sub>2</sub>S<sub>3</sub> in the order of

$10^4 \text{ cm}^{-1}$  enables it to serve as a highly efficient absorbing layer for sunlight, as shown in Figure 8a [27]. Such an effective absorber might be also beneficial for constructing laser thermal lithography resist [85], whose transparent level could be proportional to the laser intensity of the metal-transparent-metal-oxide system [86], while the obtained pattern might be grayscale and useful for the photomask on 3D lithography [86]. These observations agree well with the first-principle calculation of the linear optical spectra response of  $\text{Bi}_2\text{S}_3$  [13], while the optical non-linearity of  $\text{Bi}_2\text{S}_3$  is important due to its relationship with the control of light in optical switching devices. Typically, the three-order nonlinear coefficient  $\chi^{(3)}$  of  $\text{Bi}_2\text{S}_3$  nanocrystal measured by Z-scan technique is at  $1.43 \times 10^{-11}$  (esu) level [87], which is smaller than the first-principle calculated value of (bulk)  $\text{Bi}_2\text{S}_3$  due to the quantum confinement effect in the nanocrystals [13].

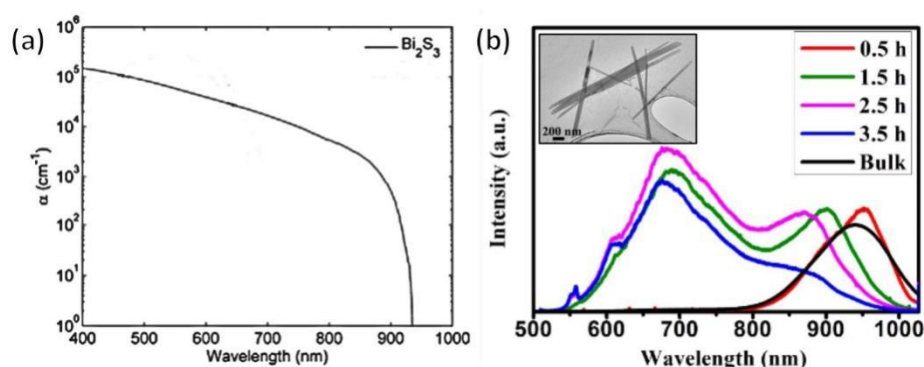


**Figure 8.** (a) Light absorption of  $\text{Bi}_2\text{S}_3$  thin film (reprinted with permission from [27] © 2022, Wiley-VCH); (b) the photoluminescence of an exfoliated  $\text{Bi}_2\text{S}_3$  nanosheet with different processing durations from 0 h to 3.5 h; the inset is the TEM image of typical exfoliated sample (reprinted with permission from [24] © 2022, American Chemical Society).

The photoluminescence (PL) of  $\text{Bi}_2\text{S}_3$  shows strong size effect, as shown in Figure 8b [24,41,88]. The studies of the samples synthesized via a high power sonication process can be taken as examples [24]: basically, the PL spectrum of bulk  $\text{Bi}_2\text{S}_3$  consists of a main peak around 946 nm, which is ascribed to the band edge emission. However, as the  $\text{Bi}_2\text{S}_3$  is high-power sonically treated for different durations from 0.5 h to 3.5 h, and accordingly exfoliated to van der Waals strings with different sizes [24], the emission from the  $\text{Bi}_2\text{S}_3$  could show the new peak centered at 685 nm along with the initial main peak, which seems to be shifted to  $\sim 900$  nm [24]. This can be attributed to the crystal defects, such as sulfur vacancies, which create deep trap states and accordingly provide alternative recombination pathways for excitonic recombination and shallowly trapped electron–hole pairs, resulting in the observed PL [24,29]. However, it is well-known that crystal defects might also increase the non-radiative recombination [89], and more physical details of the shifted-peak should be revealed by combining with other characterizations, such as absorption spectra and/or photo-carrier relaxing kinetics [90]. Further-exfoliated nanoribbons of  $\text{Bi}_2\text{S}_3$  have been inserted with oxide atoms resulting in a marked reduction in the bulky band edge emission [24,29]. The CVD-grown and hydrothermal synthesized  $\text{Bi}_2\text{S}_3$  nanosheet and nanorod also show similar new a PL peak around 624 nm beyond the band gap of bulk  $\text{Bi}_2\text{S}_3$  [16,38]. Likewise,  $\text{Bi}_2\text{S}_3$  nanoparticles prepared by reflux method could produce a PL peak near 580 nm even larger than the band gap of bulk  $\text{Bi}_2\text{S}_3$  [16].

The Raman spectra of  $\text{Bi}_2\text{S}_3$  mainly locates within the range of  $30\text{--}300 \text{ cm}^{-1}$  [78] (see Table 4). Most observed phonons are  $A_g$  and  $B_{1g}$  modes; there are two major peaks observable in some samples (Figure 9a), which are contributed by transverse  $A_g$  mode at  $237.2 \text{ cm}^{-1}$  and longitudinal  $B_{1g}$  vibration mode at  $260.7 \text{ cm}^{-1}$  revealed by first-principle calculation [78]. Actually, the wave number differences between the theoretical calculations and the experiment observations could be less than  $5 \text{ cm}^{-1}$  (Figure 9b). However, the Raman modes of the 2D nanosheets would unanimously shift toward higher wave

numbers when compared with bulk  $\text{Bi}_2\text{S}_3$  samples [24,29]. Such a shift can be associated with decreased long-range Coulombic interaction in few-layers nanosheets [29]. Moreover, due to the breaking of symmetry in bulk or nanostructures that can occur as a result of displacement defects in the lattice, which allows for the relaxation of Raman selection rules, some infrared (IR)-only mode could become Raman-active [78], resulting in the emergence of new peaks. Additionally, the peaks of some modes could occur with broadened FWHM, similarly to the observations in other bismuth compounds [61]. Moreover,  $\text{Bi}_2\text{S}_3$  tend to be thermally oxidized by annealing [57], and therefore the laser-heating effect during Raman characterization should be carefully considered. The temperature-dependent Raman spectrum shows that the  $\text{Bi}_2\text{S}_3$  nanostructure (e.g., nested nanonetwork) could be thermally -stable under 500 K [22]. However, at a higher temperature of  $\sim 573$  K, thermal oxidization would occur [57], resulting in the variations of the optical properties, such as band-edge emission reduction due to oxygen-atom insertion into the 2D  $\text{Bi}_2\text{S}_3$  nanosheet after long-term exfoliation [24].

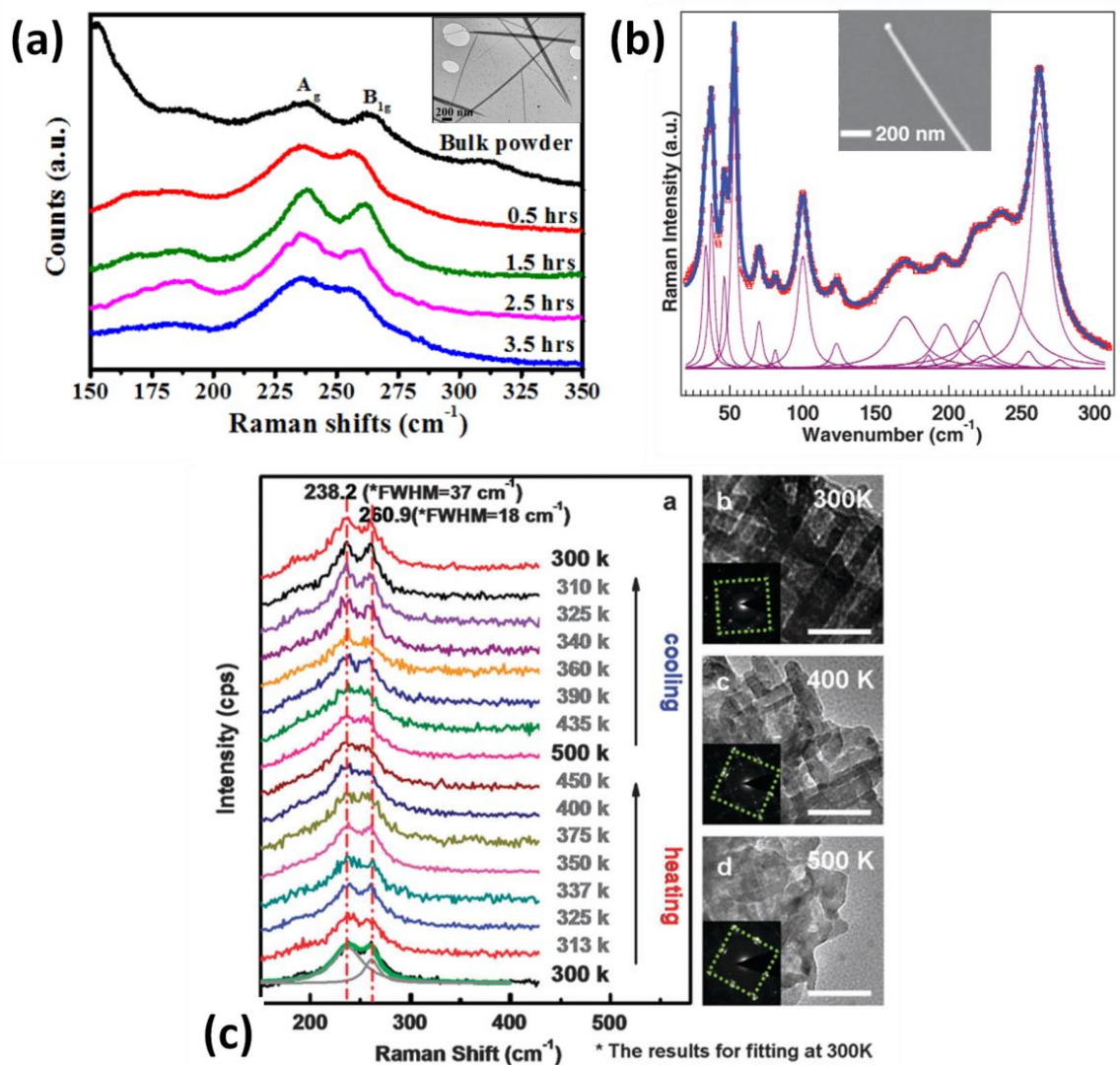


**Figure 9.** (a) Raman spectra of exfoliated  $\text{Bi}_2\text{S}_3$  nanosheet with different processing durations from 0 h to 3.5 h; the inset is a TEM image of a typical exfoliated sample (reprinted with permission from [24] © 2022, American Chemical Society); (b) comparison of first-principle calculation and experiment observation of the Raman spectra of  $\text{Bi}_2\text{S}_3$  nanowire (inset) (reprinted with permission from [24] © 2022, American Physical Society); (c) temperature-dependent Raman spectra of BSNNN (reprinted with permission from [22] © 2022, Royal Society of Chemistry).

**Table 4.** Raman frequencies and corresponding phonon modes in Bi<sub>2</sub>S<sub>3</sub> [78].

Raman Modes	Theoretical Peak Site (cm <sup>-1</sup> )	Experimental Peak Site (cm <sup>-1</sup> )
B <sub>1g</sub>	32.8	33.6
B <sub>2g</sub>	38.1	37.6
A <sub>g</sub>	40.4	46.3
A <sub>g</sub>	53.5	53.1
A <sub>g</sub>	70.9	70.1
B <sub>1g</sub>	86.0	81.1
A <sub>g</sub>	99.3	100.0,
B <sub>1g</sub>	173.4	168.7
A <sub>g</sub>	184.0	186.0, 187 <sup>a</sup> , 190.2 <sup>b</sup>
A <sub>g</sub>	195.5	196.0
A <sub>g</sub>	211.1	218.7
B <sub>3g</sub>	228.2	224.1
A <sub>g</sub>	237.2	237.1, 237 <sup>a</sup> , 235.4 <sup>b</sup> , 235 <sup>c</sup> , 238.2 <sup>d</sup>
A <sub>g</sub>	253.3	254.5
B <sub>1g</sub>	260.7	262.4, 264 <sup>a</sup> , 262.4 <sup>b</sup> , 263 <sup>c</sup> , 260.9 <sup>d</sup>
B <sub>1g</sub>	277.3	276.3

All the theoretically and experimentally observed Raman frequencies and corresponding phonon modes are from Ref. [78], except the marked data: a from Ref. [29], b from Ref. [18], c from Ref. [24], and d from Ref. [22].

#### 4. Applications

In early years, Bi<sub>2</sub>S<sub>3</sub> nanostructures were considered as interesting candidates for applications in fields such as thermoelectricity and light-absorption layers [31,35]. More recently, the special optical and electronic properties of Bi<sub>2</sub>S<sub>3</sub> have appealed to applications in new fields, such as photocatalysis, photodetection, solar energy conversion, optical-switching, and biology [4,22,43,91]. As this review is concerned with the optoelectronics of nano-Bi<sub>2</sub>S<sub>3</sub>, here we mainly discuss its representative optoelectronic applications, including photodetection, solar cells and photocatalysis.

##### 4.1. Photodetection

As typical binary V-VI semiconductors, bismuth chalcogenides of Bi<sub>2</sub>X<sub>3</sub> (X = S, Se, Te) are a category of distinctive photoresponsive materials, owing to their environment-friendly chemical compositions and dramatic optical, electrical, and photoelectric conversion characteristics [3,4,22,43,91]. Among them, Bi<sub>2</sub>S<sub>3</sub> is provided with an optimal band gap of 1.3–1.7 eV and high absorption coefficient of 10<sup>4</sup>–10<sup>5</sup> cm<sup>-1</sup> and has become a promising candidate for photodetection (Table 5) [91]. The responsive spectral range of nano-Bi<sub>2</sub>S<sub>3</sub> for photodetection is from visible to the near-infra band [17,22]. In most cases, the on/off ratio of the nano-Bi<sub>2</sub>S<sub>3</sub> photodetector could be higher than 100 [44,92], however, perhaps due to the existence of plentiful carrier traps, the temporal response of some samples is at the level of a few seconds [18,71,93,94], far from the requirements of real-time imaging, which uses speeds of, e.g., 30 frames per second (FPS). Rational trap-passivation by post-processing and junction barrier modification, as well as improving the crystalline quality or introducing heterogeneous structures, could markedly shorten the response time to sub-ms or even tens μs [23,50,95]. The high-quality nano-Bi<sub>2</sub>S<sub>3</sub> flexible photodetector developed by H. Yu et.al. shows 10 μs rise time and 350 μs decay time (Figure 10a–d) [23,95]. Ref. [50] proposes a single-nanowire-device, in which Bi<sub>2</sub>S<sub>3</sub> NW is surface-oxidated to fill the vacancies of sulfur with oxygen atoms and in situ form a Bi<sub>2</sub>S<sub>3</sub>/Bi<sub>2</sub>S<sub>3-x</sub>O<sub>x</sub> heterojunction (Figure 10e–h). Such a heterojunction could not only maintain good response time

at sub-ms level at visible range, but also achieve rather high responsivity (2908.9 A/W) and detectivity ( $\sim 10^{11}$  Jones), as shown in Figure 10i–l. The improvement of the overall detection performances of such a  $\text{Bi}_2\text{S}_3/\text{Bi}_2\text{S}_{3-x}\text{O}_x$  heterojunction might be attributed to two factors: (1) the  $\text{Bi}_2\text{S}_3$  and  $\text{Bi}_2\text{S}_{3-x}\text{O}_x$  are *n*-type and *p*-type, respectively, and accordingly, the intrinsic electrical field of PN junction enables accelerated carrier motion [96]; (2) other than the junctions such as  $\text{Bi}_2\text{S}_3/\text{BiOX}$  ( $X = \text{Cl}, \text{I}$ ) [21,61,71], the proposed  $\text{Bi}_2\text{S}_3/\text{Bi}_2\text{S}_{3-x}\text{O}_x$  system has better lattice matching, which reduces the interface defects.

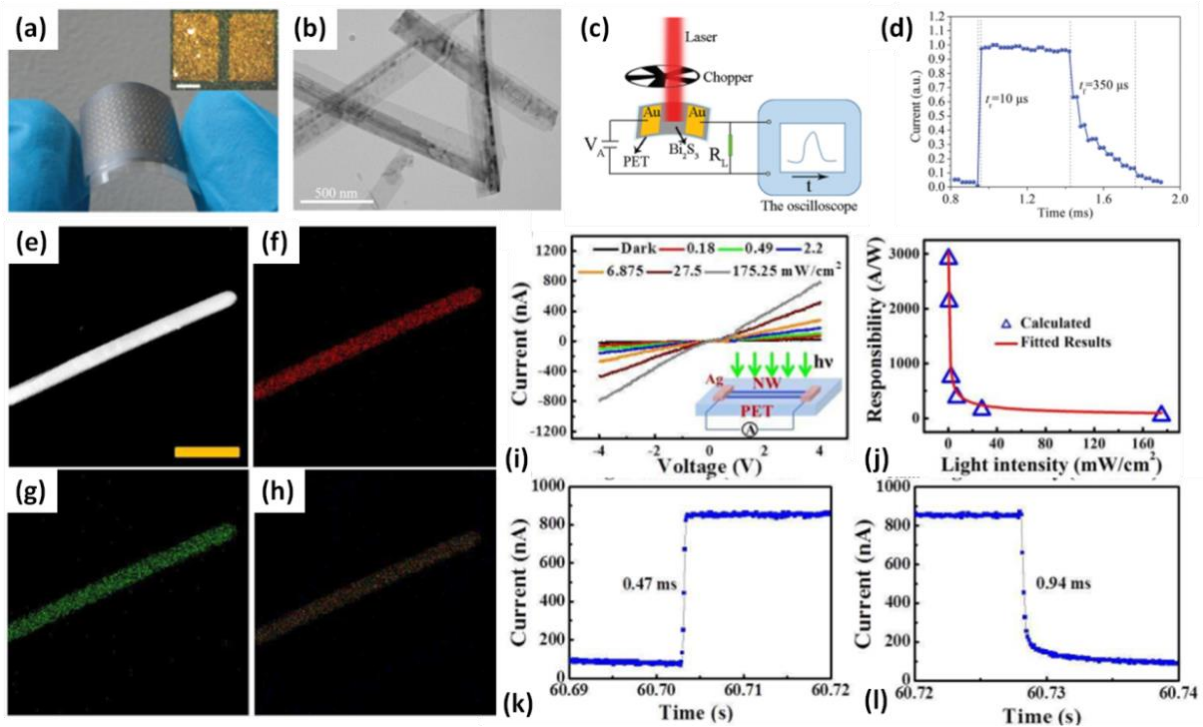


**Figure 10.** (a) Flexible  $\text{Bi}_2\text{S}_3$  nanosheet film photodetector and its (b) TEM image; (c) experiment setup for photodetector characterization; (d) rise and decay time of photodetector based-on  $\text{Bi}_2\text{S}_3$  nanosheet film. (Reprinted with permission from [95] © 2022, Wiley-VCH). (e)  $\text{Bi}_2\text{S}_3/\text{Bi}_2\text{S}_{3-x}\text{O}_x$  nanowire and its (f) S-, (g) Bi- and (h) O- element mapping; (i) light-intensity dependent I-V characteristics, (j) responsivity, (k) rise- and (l) decay-time of single  $\text{Bi}_2\text{S}_3/\text{Bi}_2\text{S}_{3-x}\text{O}_x$  nanowire photodetector. (Reprinted with permission from [50] © 2022, Elsevier).

#### 4.2. Photovoltaic Cell

As mentioned above,  $\text{Bi}_2\text{S}_3$  is a binary chalcogenide semiconductor with single phase and fixed composition. It inspires the exploration as a promising absorber material for solar energy (Table 6). This is because on one hand, its direct bandgap of 1.3~1.7 eV lies within the optimal bandgap value for the single junction solar cell, while on the other hand,  $\text{Bi}_2\text{S}_3$  has a high absorption coefficient (at wavelengths of approximately 600 nm) and relatively high carrier mobility, enabling full light absorption and photogenerated carrier collection within a film thickness of, typically, a few micrometers [26]. In addition, the raw materials (Bi and S) are low-cost and non-toxic. All the above features make  $\text{Bi}_2\text{S}_3$  a candidate for solar absorbers. Moreover, beyond the regular light-absorption function, nano- $\text{Bi}_2\text{S}_3$  in solar cells could serve as a number of other roles, such as the electron acceptor for organic or inorganic heterojunction solar cells, the media for dye- or quantum-dot-sensitization, and the electron transport layer for perovskite solar cells [14,26,37,45,97]. It seems that the regular PN junction structure using  $\text{Bi}_2\text{S}_3$  as the *n*-layer cannot produce a practical performance for solar-cell application. Typical conversion efficiency is less than 1% [36,45,70,98–102], while state-of-art quantum dot-sensitized solar cells (QDSSCs) with  $\text{Bi}_2\text{S}_3$  quantum dots could achieve conversion efficiency higher than 3% (Figure 11a,b) [14,103]. The hybridization

strategy, e.g., Bi<sub>2</sub>S<sub>3</sub> nanowire networks/P3HT hybrid solar cells, or Bi<sub>2</sub>S<sub>3</sub>/TiO<sub>2</sub> cross-linked-structure, could further improve the conversion efficiency [37,103]. Besides its use as a conversion media, Bi<sub>2</sub>S<sub>3</sub> could also be a promising electron transport layer for perovskite solar cells (Figure 11c); the NiO/CH<sub>3</sub>NH<sub>3</sub>PbI<sub>3</sub>/Bi<sub>2</sub>S<sub>3</sub> system could achieve conversion efficiency of 13% (Figure 11d) [26].

**Table 5.** Selected reports on the nano-Bi<sub>2</sub>S<sub>3</sub>-based photodetector.

Samples	Wavelength	I <sub>on</sub> /I <sub>off</sub>	Temporal Response (Rise/Decay)	Responsivity
Bi <sub>2</sub> S <sub>3</sub> nano-networks [18]	671 nm	/	~3 s	/
Hierarchical Bi <sub>2</sub> S <sub>3</sub> nanostructures [91]	/	/	50/240 ms	/
Bi <sub>2</sub> S <sub>3</sub> /Bi <sub>2</sub> S <sub>3-x</sub> O <sub>x</sub> nanowire [50]	475–650 nm	44.6	0.47/0.93 ms	2908.9 A/W
Bi <sub>2</sub> S <sub>3</sub> nanocrystalline [47]	/	/	23 ms	/
Bi <sub>2</sub> S <sub>3</sub> /BiOCl composites [99]	/	330	70 ms	/
Bi <sub>2</sub> S <sub>3</sub> nanorod [23,95]	405 to 780 nm	/	10/350 μs	4.4 A/W
Bi <sub>2</sub> S <sub>3</sub> /SnS heterojunction thin film [93]	400 to 800 nm	/	~50 s	/
Bi <sub>2</sub> S <sub>3</sub> nanorods and nanoflowers [44]	Laser@809 nm and 980 nm	~100	2/3 s	/
Bi <sub>2</sub> S <sub>3</sub> thin film [70]	650 nm	/	67.8 ms	/
Dandelion-shaped hierarchical Bi <sub>2</sub> S <sub>3</sub> microsphere [92]	650 nm	567	~10 s	/
Bi <sub>2</sub> S <sub>3</sub> /BiOI p-n heterojunction [71]	visible	/	~5 s	/
Bi <sub>2</sub> S <sub>3</sub> Nanorods [94]	475 nm/550 nm/650 nm	/	~5 s	/

**Table 6.** Selected reports on the nano-Bi<sub>2</sub>S<sub>3</sub>-based solar cell.

Sample	V <sub>oc</sub> (V)	J <sub>sc</sub> (mA/cm <sup>2</sup> )	Filing Factor	Conversion Efficiency (%)
Bi <sub>2</sub> S <sub>3</sub> /PbS thin film [99]	0.13–0.31	0.5–5	0.25–0.42	0.1–0.4
Bi <sub>2</sub> S <sub>3</sub> /PbS thin film [100]	0.28	2.1	0.34	0.19
Bi <sub>2</sub> S <sub>3</sub> thin film [70]	0.23	10	0.33	0.75
Bi <sub>2</sub> S <sub>3</sub> quantum dot-sensitized TiO <sub>2</sub> solar cells [98]	0.502	7.9	0.537	2.52
Bi <sub>2</sub> S <sub>3</sub> nanowire networks/P3HT hybrid solar cells [37]	0.7	10.7	0.45	3.3
Bi <sub>2</sub> S <sub>3</sub> /P3OT solar cells [104]	0.44	0.022	/	/
BiOI/Bi <sub>2</sub> S <sub>3</sub> heterojunction films [101]	0.5	1.82	0.4	0.36
TiO <sub>2</sub> /Bi <sub>2</sub> S <sub>3</sub> heterostructure [102]	0.33	0.57	0.39	0.148
Bi <sub>2</sub> S <sub>3</sub> nanocrystal film [45]	0.058	0.33	0.283	0.0054
Bi <sub>2</sub> S <sub>3</sub> colloidal nanocrystals [36]	0.36	3.21	0.52	0.60
Polymer/Bi <sub>2</sub> S <sub>3</sub> nanocrystal solar cells [27]	0.32	3	0.49	0.46
Bi <sub>2</sub> S <sub>3</sub> /TiO <sub>2</sub> cross-linked heterostructure [103]	0.48	14.48	0.47	3.29
Bi <sub>2</sub> S <sub>3</sub> /TiO <sub>2</sub> nanotube array cell [75]	0.766	1.56	0.602	0.718
NiO/CH <sub>3</sub> NH <sub>3</sub> PbI <sub>3</sub> /Bi <sub>2</sub> S <sub>3</sub> solar cell [26]	0.949	18.6	74.2	13
Bi <sub>2</sub> S <sub>3</sub> quantum dots/TiO <sub>2</sub> nanorod QDSSC [14]	0.46	14.51	0.46	3.06

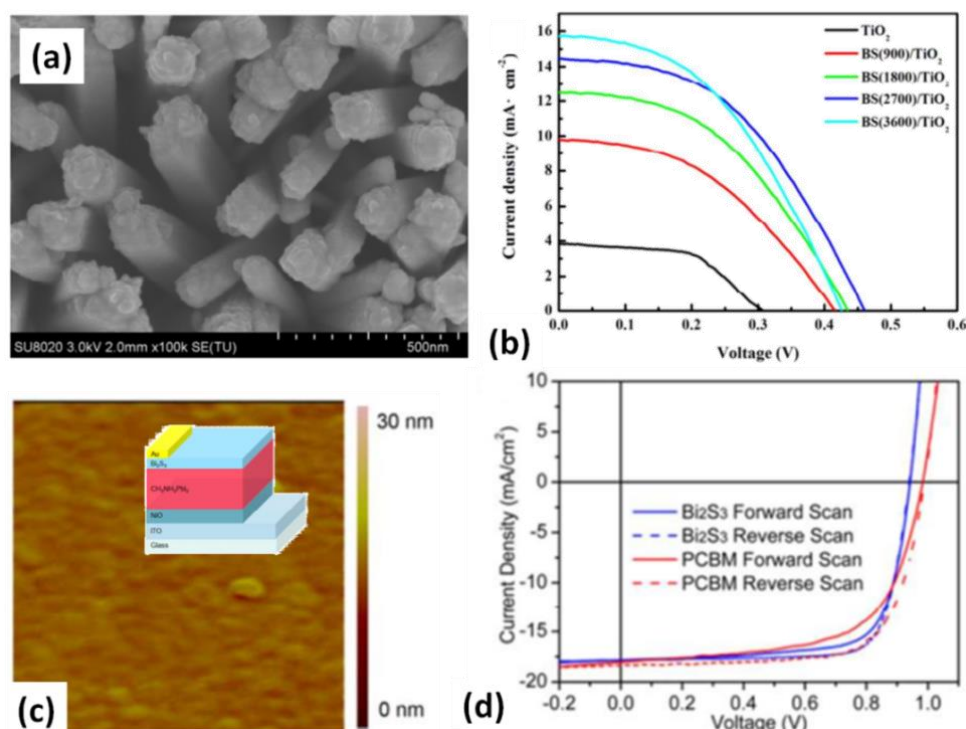


**Figure 11.** (a) Bi<sub>2</sub>S<sub>3</sub> quantum dots coated on TiO<sub>2</sub> nanrod by PLD; (b) photo-voltaic characteristic of Bi<sub>2</sub>S<sub>3</sub> quantum dot-sensitized TiO<sub>2</sub> solar cells; (reprinted with permission from [14] © 2022, Royal Society of Chemistry). (c) Low-roughness Bi<sub>2</sub>S<sub>3</sub> thin film deposited on CH<sub>3</sub>NH<sub>3</sub>PbI<sub>3</sub> by thermal evaporation as electron transport layer; (d) the photo-voltaic characteristic of the NiO/CH<sub>3</sub>NH<sub>3</sub>PbI<sub>3</sub>/Bi<sub>2</sub>S<sub>3</sub> solar cell. (Reprinted with permission from [26] © 2022, American Chemical Society).

To summarize the studies on nano-Bi<sub>2</sub>S<sub>3</sub> in solar cells, this system so far seems not to have fully realized its potential. The non-practical conversion efficiency may be limited by superficial defects in the Bi<sub>2</sub>S<sub>3</sub> [22]. In addition, on the viewpoint of material, as a semiconductor already possessing an optimal photovoltaic band gap, when Bi<sub>2</sub>S<sub>3</sub> is processed into nanoscale, it might help to produce photon-conversion sites, but on the other hand it is also critical to avoid band-misalignment due to the unnecessary increase in the band gap brought by quantum confinement in the nanostructures [7]. Rational trade-off among different aspects, including carrier mobility, carrier concentration, photon-conversion site (area of junction for electron-hole pair generation and separation), and band alignment would be quite critical for the further progress of the nano-Bi<sub>2</sub>S<sub>3</sub>-based solar cell.

#### 4.3. Photocatalysis

Photocatalysis is one of most active research fields focused on the applications of Bi<sub>2</sub>S<sub>3</sub> nanostructures, with hundreds of reports published within a few years [16,69,105]. The interest in this field is based in particular on the low cost and low toxicity of Bi, which has been named “green metal” by some authors, as well as its several compounds, including Bi<sub>2</sub>S<sub>3</sub> [58,61,74]. Table 7 presents a selection of references where the photocatalytic properties of Bi<sub>2</sub>S<sub>3</sub>-based materials were studied, and specifies the chemical reactions that were considered.

**Table 7.** Selected reports on the nano-Bi<sub>2</sub>S<sub>3</sub>-based photocatalyst.

Sample	Photocatalytic Reaction	Spectral Region
TiO <sub>2</sub> nanotubes/Bi <sub>2</sub> S <sub>3</sub> -BiOI [71]	RhB, methyl orange (MO), methylene blue (MB) and Cr (VI)	Visible (Xe lamp)
Bi <sub>2</sub> S <sub>3</sub> nanoparticles [16]	MB	Visible
Bi <sub>2</sub> S <sub>3</sub> microsphere [65]	MO	Visible
Bi <sub>2</sub> S <sub>3</sub> nanorod [4]	MB, MO, RhB	UV
Bi <sub>2</sub> S <sub>3</sub> nanoparticles [59]	CO <sub>2</sub>	Visible (mercury lamp)
Bi <sub>2</sub> S <sub>3</sub> /Bi <sub>2</sub> WO <sub>6</sub> hierarchical microstructures [72]	Ofloxacin	Visible
Bi <sub>2</sub> S <sub>3</sub> /ZnS microspheres [73]	RhB, oxytetracycline (OTC)	Visible
CuS-Bi <sub>2</sub> S <sub>3</sub> hierarchical architectures [77]	Rh-B and crystal violet (CV)	Visible
Bi <sub>2</sub> S <sub>3</sub> @ZIF-8 core-shell heterostructure [52]	RhB	Visible
Bi <sub>2</sub> S <sub>3</sub> nanoribbons [58]	CO <sub>2</sub>	Visible
Bi <sub>2</sub> O <sub>3</sub> /Bi <sub>2</sub> S <sub>3</sub> /MoS <sub>2</sub> n-p heterojunction [58]	Oxidizing water molecules, MB	Simulated solar light
Bi <sub>2</sub> S <sub>3</sub> nanorods [69]	RhB	UV-vis
Bi <sub>2</sub> S <sub>3</sub> /Bi <sub>2</sub> O <sub>2</sub> CO <sub>3</sub> heterojunction [74]	RhB	Visible (Xe lamp)

The pioneering works on this topic demonstrated that Bi<sub>2</sub>S<sub>3</sub> nanostructures can act as direct photocatalysts [4,69]. In [69], solution-processed Bi nanowires diluted in water were used as the catalyst for RhB removal. A solution of RhB was degraded under visible light within 4 h. Afterward, the degradation of MO and MB was also demonstrated (Figure 12a) [4]. Besides the exploration on dye-removal, nano-Bi<sub>2</sub>S<sub>3</sub> (nanoparticles, microspheres, thin urchin-like Bi<sub>2</sub>S<sub>3</sub> spheres, and nanoribbon) was also able to reduce CO<sub>2</sub> to methyl and methanol (Figure 12b) [58,59]. As mentioned above, Bi<sub>2</sub>S<sub>3</sub> nanostructures efficiently adsorb the incident light, which can be converted to photocarriers that migrate to the nanostructure surface, hence they can ease the formation of intermediates, accelerating chemical reactions. Thus, the high absorption capability of Bi<sub>2</sub>S<sub>3</sub> certainly plays a key role in this process, because it enables a significant optical absorption efficiency that is required for the efficient generation of photocarriers. Moreover, other than the ~1.3 eV band gap of bulk Bi<sub>2</sub>S<sub>3</sub>, the nano-structured Bi<sub>2</sub>S<sub>3</sub> could have varied band structure, and accordingly achieve tunable photocatalytic response spectral range under visible light and also UV [4,69]. Furthermore, it is noteworthy that the potential of the photogenerated electrons (holes) must be low (high) enough so that they can efficiently trigger the chemical reaction of interest, and this potential is defined by the photon energy of the incident photons. Hence, the hybrid structure of other materials (TiO<sub>2</sub>, Bi<sub>2</sub>WO<sub>6</sub>, Bi<sub>2</sub>O<sub>2</sub>CO<sub>3</sub>, Bi<sub>2</sub>O<sub>3</sub>, ZIF-8, ZnS, CuS) with nano-Bi<sub>2</sub>S<sub>3</sub> could enhance catalysis performances. Accordingly, the co-catalysis by such hybrid structures seems more promising for the degradation of RhB, CV, MO, MB, and ofloxacin [52,58,71–74,77].

The photocatalysis mechanism of nano-Bi<sub>2</sub>S<sub>3</sub> suggested by experimental results varied from one work to another (together with the nature and structure of the hybrid material), however, some evidence highlighted in these studies can be extracted. On one hand, Bi<sub>2</sub>S<sub>3</sub> nanostructures allow photocatalytic capabilities in the visible region due to their rational band gap and strong optical absorption efficiency. On the other hand, depending on the electronic configuration of the hybrid (including the potential of the photocarriers in Bi<sub>2</sub>S<sub>3</sub> nanostructure, location of the conduction, and valence band of the semiconductor), photocarriers, especially electrons, can flow from the Bi<sub>2</sub>S<sub>3</sub> nanostructure to the hybrid semiconductor or the opposite. In other words, according to these different reports, nano-Bi<sub>2</sub>S<sub>3</sub> can act as an electron donor (the electrons being made available for reactions at the surface of the semiconductor, Figure 12c) or as electron acceptor (the electrons provided by the semiconductor reacting at their surface, Figure 12d) [49,52,73]. Thus, further studies

would be of significance to understand the mechanism of the photocatalyst based on nano-Bi<sub>2</sub>S<sub>3</sub>, as well as related hybrid structures.

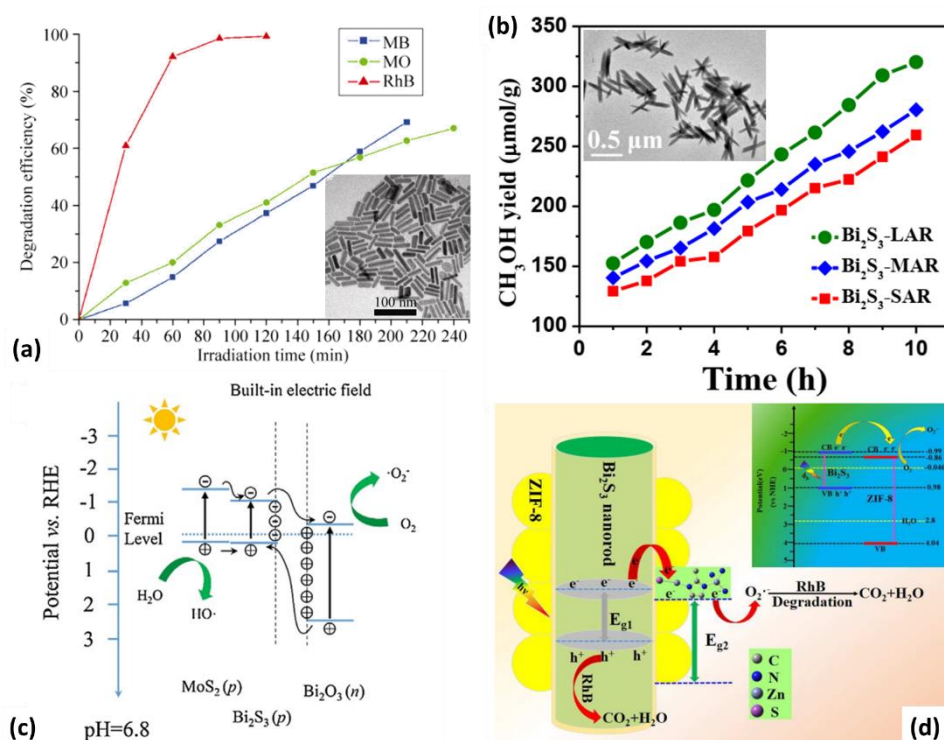


**Figure 12.** (a) Dye removal photo-catalyzed by Bi<sub>2</sub>S<sub>3</sub> nanorod (reprinted with permission under CC-BY-NC 2.0 from [10] © 2022); (b) CO<sub>2</sub> reduction photo-catalyzed by Bi<sub>2</sub>S<sub>3</sub> nano-ribbon (reprinted with permission from [58] © 2022, Elsevier); (c) proposed photo-catalytic mechanism of Bi<sub>2</sub>O<sub>3</sub>/Bi<sub>2</sub>S<sub>3</sub>/MoS<sub>2</sub> n-p heterojunction where Bi<sub>2</sub>S<sub>3</sub> act as an electron acceptor (reprinted with permission from [49] © 2022, Elsevier); (d) proposed mechanism for the photo-catalytic degradation of RhB where the Bi<sub>2</sub>S<sub>3</sub> nanorod acts as an electron donor (reprinted with permission from [52] © 2022, Royal Society of Chemistry).

### 5. Conclusions and Perspectives

Bi<sub>2</sub>S<sub>3</sub> has motivated and attracted the interest of scientists during the past decades due to its potential in thermoelectric and hydrogen storage and its Li- and Na- ion battery properties. Furthermore, Bi<sub>2</sub>S<sub>3</sub> has recently become appealing for applications involving its particular optoelectronic properties. Increasing interest has been paid especially to its application in photodetection, solar energy conversion, and photocatalysts. In this article, we present a comprehensive review of the recent advances on this field: electrical and optical properties of Bi<sub>2</sub>S<sub>3</sub>, growth of Bi<sub>2</sub>S<sub>3</sub> nanostructures, and emerging optoelectronic applications. Bi<sub>2</sub>S<sub>3</sub> nanostructures with a broad variety of sizes and shapes can be prepared with different existing fabrication methods:

- (1) Vapor phase deposition, involving thermal evaporation, LP-MOCVD, and PLD; mainly used to prepare thin film.
- (2) Liquid phase deposition, involving chemical bath or electrochemical deposition, is also used to fabricate thin film.
- (3) Surface sulfurization can produce nano-Bi<sub>2</sub>S<sub>3</sub> with better crystalline quality, but requires high processing temperature.
- (4) Chemical synthesis Bi<sub>2</sub>S<sub>3</sub> nanostructures with a broad variety of shapes from 0D to 3D, as well as the hierarchical and heterogeneous structures of Bi<sub>2</sub>S<sub>3</sub>.

Optimal band gap, high light absorption, and good carrier mobility concentration make nano-Bi<sub>2</sub>S<sub>3</sub> feasible for a series of optoelectronic applications, but better controlled

crystalline quality, nanostructure size, shape, and environment is desired. The SOC effects could be critical to further extend the design space of the (linear) optical response, while rational doping could help to improve the nonlinear optical properties and consequently produce more promising nonlinear optical materials [13]. However, there are still amount of works to achieve better nano-Bi<sub>2</sub>S<sub>3</sub> optoelectronics. In most of the works that we have discussed, the influence of the crystal facets exposed at the surface of the Bi<sub>2</sub>S<sub>3</sub> nanostructures on their optoelectronic functionalities has not been thoroughly evaluated. In addition, because of the structural and electronic anisotropy of nano-Bi<sub>2</sub>S<sub>3</sub> and its facet-dependent surface states [29], the nature of the exposed facets might affect either the optical response of nano-Bi<sub>2</sub>S<sub>3</sub> with a high surface-to-volume ratio (where surface states play a significant role on the overall response) or their functionalities for applications in which surfaces are a key player (such as catalysis, surface-enhanced Raman spectroscopy, and charge transport). However, emerging photodetector, solar cells, and photocatalysts based on nano-Bi<sub>2</sub>S<sub>3</sub> clearly show great potential in optoelectronics. Besides these applications, further opportunities for nano-Bi<sub>2</sub>S<sub>3</sub> in this field may lie in the switchable optical device, the bolometer, and beyond [85].

In sum, the progress on the fabrication of Bi<sub>2</sub>S<sub>3</sub> nanostructures, the control and understanding of their excellent optoelectronic responses, and the emergence of alternative applications open new possibilities for nano-Bi<sub>2</sub>S<sub>3</sub> beyond the already-explored paths. More experimental observations are needed to realize its optical potential. Further developments are also necessary to overcome the obstacles and highlight the unsolved issues to achieve more practical nano Bi<sub>2</sub>S<sub>3</sub>-based optical materials and devices.

**Author Contributions:** Conceptualization, Y.T. and Z.L.; writing—original draft preparation, Y.T.; writing—review and editing, Y.T. and Z.L. All authors have read and agreed to the published version of the manuscript.

**Funding:** This research was supported by the Scientific Research Fund of Hunan Provincial Education Department (No.20C0367, No.19B100) and Hunan Provincial Natural Science Fund (2019JJ50025).

**Data Availability Statement:** All data included in this study are available upon request by contact with the corresponding author.

**Conflicts of Interest:** The authors declare no conflict of interest.

## References

1. Popescu, M. Chalcogenides—Past, present, future. *J. Non-Cryst. Solids* **2006**, *352*, 887–891. [[CrossRef](#)]
2. Sousa, V. Chalcogenide materials and their application to Non-Volatile Memories. *Microelectron. Eng.* **2011**, *88*, 807–813. [[CrossRef](#)]
3. Moore, J.E. The birth of topological insulators. *Nature* **2010**, *464*, 194–198. [[CrossRef](#)] [[PubMed](#)]
4. Wu, T.; Zhou, X.; Zhang, H.; Zhong, X. Bi<sub>2</sub>S<sub>3</sub> nanostructures: A new photocatalyst. *Nano Res.* **2010**, *3*, 379–386. [[CrossRef](#)]
5. Sanghera, J.S.; Shaw, L.B.; Aggarwal, I.D. Chalcogenide Glass-Fiber-Based Mid-IR Sources and Applications. *IEEE J. Sel. Top. Quantum Electron.* **2009**, *15*, 114–119. [[CrossRef](#)]
6. Toudert, J.; Serna, R. Interband transitions in semi-metals, semiconductors, and topological insulators: A new driving force for plasmonics and nanophotonics [Invited]. *Opt. Mater. Express* **2017**, *7*, 2299–2325. [[CrossRef](#)]
7. Tian, Y.; Toudert, J. Nanobismuth: Fabrication, Optical, and Plasmonic Properties—Emerging Applications. *J. Nanotechnol.* **2018**, *2018*, 3250932. [[CrossRef](#)]
8. Panmand, R.P.; Kulkarni, M.V.; Valant, M.; Gosavi, S.W.; Kale, B.B. Quantum confinement of Bi<sub>2</sub>S<sub>3</sub> in glass with magnetic behavior. *AIP Adv.* **2013**, *3*, 022123. [[CrossRef](#)]
9. Yang, Y.; Xu, Z.; Sheng, L.; Shen, R.; Xing, D.Y. Magnetoresistance in an ultrathin Bi<sub>2</sub>Se<sub>3</sub> film between two ferromagnetic insulators. *Appl. Phys. Lett.* **2011**, *99*, 182101. [[CrossRef](#)]
10. Lu, C.; Li, Z.; Yu, L.; Zhang, L.; Xia, Z.; Jiang, T.; Yin, W.; Dou, S.; Liu, Z.; Sun, J. Nanostructured Bi<sub>2</sub>S<sub>3</sub> encapsulated within three-dimensional N-doped graphene as active and flexible anodes for sodium-ion batteries. *Nano Res.* **2018**, *11*, 4614–4626. [[CrossRef](#)]
11. Zhao, Y.; Gao, D.; Ni, J.; Gao, L.; Yang, J.; Dongliang, Y. One-pot facile fabrication of carbon-coated Bi<sub>2</sub>S<sub>3</sub> nanomeshes with efficient Li-storage capability. *Nano Res.* **2014**, *7*, 765–773. [[CrossRef](#)]
12. Chang, Y.; Yang, Q.L.; Guo, J.; Feng, J.; Ge, Z.H. Enhanced thermoelectric properties of Bi<sub>2</sub>S<sub>3</sub> polycrystals through an electroless nickel plating process. *RSC Adv.* **2019**, *9*, 23029–23035. [[CrossRef](#)] [[PubMed](#)]
13. Ben Abdallah, H.; Ouerghui, W. Spin-orbit coupling effect on electronic, linear and nonlinear optical properties of Bi<sub>2</sub>S<sub>3</sub> and the ternary bismuth sulfide Bi<sub>2</sub>S<sub>2.75</sub>Se<sub>0.25</sub>: Ab-initio calculations. *Opt. Quantum Electron.* **2021**, *54*, 20. [[CrossRef](#)]

14. Han, M.; Guo, H.; Li, B.; Jia, J.; Wang, W. Controllable coverage of Bi<sub>2</sub>S<sub>3</sub> quantum dots on one-dimensional TiO<sub>2</sub> nanorod arrays by pulsed laser deposition technique for high photoelectrochemical properties. *New J. Chem.* **2017**, *41*, 4820–4827. [[CrossRef](#)]
15. Arabzadeh, A.; Salimi, A. Facile Synthesis of Ultra-wide Two Dimensional Bi<sub>2</sub>S<sub>3</sub> Nanosheets: Characterizations, Properties and Applications in Hydrogen Peroxide Sensing and Hydrogen Storage. *Electroanalysis* **2017**, *29*, 2027–2035. [[CrossRef](#)]
16. Arumugam, J.; Raj, A.D.; Irudayaraj, A.A. Solvent effects on the properties of Bi<sub>2</sub>S<sub>3</sub> nanoparticles: Photocatalytic application. *J. Mater. Sci. Mater. Electron.* **2017**, *28*, 3487–3494. [[CrossRef](#)]
17. Chitara, B.; Kolli, B.S.; Yan, F. Near-Infrared Photodetectors Based on 2D Bi<sub>2</sub>S<sub>3</sub>. *Chem. Phys. Lett.* **2022**, *804*, 139876. [[CrossRef](#)]
18. Tian, Y.; Zhang, S.; Tan, W. Improved optical and electrical switching in Bi<sub>2</sub>S<sub>3</sub> nested nano-networks with broad trap distribution. *Appl. Nanosci.* **2022**, *12*, 2023–2030. [[CrossRef](#)]
19. Tian, Y.; Pan, L.; Guo, C.F.; Liu, Q. Atomic origin of the traps in memristive interface. *Nano Res.* **2017**, *10*, 1924–1931. [[CrossRef](#)]
20. Schricker, A.D.; Sigman, M.B., Jr.; Korgel, B.A. Electrical transport, Meyer–Neldel rule and oxygen sensitivity of Bi<sub>2</sub>S<sub>3</sub> nanowires. *Nanotechnology* **2005**, *16*, S508. [[CrossRef](#)]
21. Stallinga, P.; Gomes, H. Trap states as an explanation for the Meyer–Neldel rule in semiconductors. *Org. Electron.* **2005**, *6*, 137–141. [[CrossRef](#)]
22. Tian, Y.; Guo, C.; Guo, S.; Yu, T.; Liu, Q. Bivariate-continuous-tunable interface memristor based on Bi<sub>2</sub>S<sub>3</sub> nested nano-networks. *Nano Res.* **2014**, *7*, 953–962. [[CrossRef](#)]
23. Tian, Y.; Guo, C.F.; Zhang, J.; Liu, Q. Operable persistent photoconductivity of Bi<sub>2</sub>S<sub>3</sub> nested nano-networks. *Phys. Chem. Chem. Phys.* **2015**, *17*, 851–857. [[CrossRef](#)] [[PubMed](#)]
24. Schricker, A.D. *Electrical Properties of Single GaAs, Bi<sub>2</sub>S<sub>3</sub> and Ge Nanowires*; University of Texas Libraries: San Antonio, TX, USA, 2005.
25. Yu, H.; Wang, J. Bismuth Sulfide (Bi<sub>2</sub>S<sub>3</sub>) Nanorods as Efficient Photodetection Materials. In Proceedings of the 2016 5th International Conference on Advanced Materials and Computer Science, Qingdao, China, 26–27 March; pp. 935–938.
26. Dhar, N.; Syed, N.; Mohiuddin, M.; Jannat, A.; Zavabeti, A.; Zhang, B.Y.; Datta, R.S.; Atkin, P.; Mahmood, N.; Esrafilzadeh, D.; et al. Exfoliation Behavior of van der Waals Strings: Case Study of Bi<sub>2</sub>S<sub>3</sub>. *ACS Appl. Mater. Interfaces* **2018**, *10*, 42603–42611. [[CrossRef](#)] [[PubMed](#)]
27. Guo, C.; Zhang, J.; Tian, Y.; Liu, Q. A General Strategy to Superstructured Networks and Nested Self-Similar Networks of Bismuth Compounds. *ACS Nano* **2012**, *6*, 8746–8752. [[CrossRef](#)]
28. Li, D.-B.; Hu, L.; Xie, Y.; Niu, G.; Liu, T.; Zhou, Y.; Gao, L.; Yang, B.; Tang, J. Low-Temperature-Processed Amorphous Bi<sub>2</sub>S<sub>3</sub> Film as an Inorganic Electron Transport Layer for Perovskite Solar Cells. *ACS Photonics* **2016**, *3*, 2122–2128. [[CrossRef](#)]
29. Martinez, L.; Bernechea, M.; de Arquer, F.P.G.; Konstantatos, G. Near IR-Sensitive, Non-toxic, Polymer/Nanocrystal Solar Cells Employing Bi<sub>2</sub>S<sub>3</sub> as the Electron Acceptor. *Adv. Energy Mater.* **2011**, *1*, 1029–1035. [[CrossRef](#)]
30. Li, L.; Sun, N.; Huang, Y.; Qin, Y.; Zhao, N.; Gao, J.; Li, M.; Zhou, H.; Qi, L. Topotactic Transformation of Single-Crystalline Precursor Discs into Disc-Like Bi<sub>2</sub>S<sub>3</sub> Nanorod Networks. *Adv. Funct. Mater.* **2008**, *18*, 1194–1201. [[CrossRef](#)]
31. Messalea, K.A.; Zavabeti, A.; Mohiuddin, M.; Syed, N.; Jannat, A.; Atkin, P.; Ahmed, T.; Walia, S.; McConville, C.F.; Kalantar-Zadeh, K.; et al. Two-Step Synthesis of Large-Area 2D Bi<sub>2</sub>S<sub>3</sub> Nanosheets Featuring High In-Plane Anisotropy. *Adv. Mater. Interfaces* **2020**, *7*, 2001131. [[CrossRef](#)]
32. Chen, X.L.; Yan, K.; Chu, H.Y. Preheating Effects on Bi<sub>2</sub>S<sub>3</sub> Morphology Synthesized via Hydrothermal Method. *Adv. Mater. Res.* **2013**, *631–632*, 298–302. [[CrossRef](#)]
33. Wang, Z.J.; Qu, S.C.; Xu, Y.; Chen, Y.H.; Zeng, X.B.; Liu, J.P.; Wu, J.; Wang, Z.G. Solventless Synthesis of Bi<sub>2</sub>S<sub>3</sub> Nanowires and their Application to Solar Cells. *Adv. Mater. Res.* **2007**, *26–28*, 601–607. [[CrossRef](#)]
34. Reynoso, Y.R.; Martinez-Ayala, A.; Pal, M.; Paraguay-Delgado, F.; Mathews, N. Bi<sub>2</sub>S<sub>3</sub> nanoparticles by facile chemical synthesis: Role of pH on growth and physical properties. *Adv. Powder Technol.* **2018**, *29*, 3561–3568. [[CrossRef](#)]
35. Gao, C.; Shen, H.; Sun, L. Preparation of nanowall Bi<sub>2</sub>S<sub>3</sub> films by chemical bath deposition. *Appl. Surf. Sci.* **2011**, *258*, 89–92. [[CrossRef](#)]
36. Maria, C.C.S.; Patil, R.A.; Hasibuan, D.P.; Saragih, C.S.; Lai, C.-C.; Liou, Y.; Ma, Y.-R. White-light photodetection enhancement and thin film impediment in Bi<sub>2</sub>S<sub>3</sub> nanorods/thin-films homojunction photodetectors. *Appl. Surf. Sci.* **2022**, *584*, 152608. [[CrossRef](#)]
37. Chen, Y.; Wang, D.; Zhou, Y.; Pang, Q.; Shao, J.; Wang, G.; Wang, J.; Zhao, L.-D. Enhancing the thermoelectric performance of Bi<sub>2</sub>S<sub>3</sub>: A promising earth-abundant thermoelectric material. *Front. Phys.* **2018**, *14*, 13601. [[CrossRef](#)]
38. Bernechea, M.; Cao, Y.; Konstantatos, G. Size and bandgap tunability in Bi<sub>2</sub>S<sub>3</sub> colloidal nanocrystals and its effect in solution processed solar cells. *J. Mater. Chem. A* **2015**, *3*, 20642–20648. [[CrossRef](#)]
39. Whittaker-Brooks, L.; Gao, J.; Hailey, A.K.; Thomas, C.R.; Yao, N.; Loo, Y.L. Bi<sub>2</sub>S<sub>3</sub> nanowire networks as electron acceptor layers in solution-processed hybrid solar cells. *J. Mater. Chem. C* **2015**, *3*, 2686–2692. [[CrossRef](#)]
40. Peter, L.M.; Wijayantha, K.U.; Riley, D.J.; Waggett, J.P. Band-edge tuning in self-assembled layers of Bi<sub>2</sub>S<sub>3</sub> nanoparticles used to photosensitize nanocrystalline TiO<sub>2</sub>. *J. Phys. Chem. B* **2003**, *107*, 8378–8381. [[CrossRef](#)]
41. Yu, Y.; Jin, C.H.; Wang, R.H.; Chen, Q.; Peng, L.M. High-Quality Ultralong Bi<sub>2</sub>S<sub>3</sub> Nanowires: Structure, Growth, and Properties. *J. Phys. Chem. B* **2005**, *109*, 18772–18776. [[CrossRef](#)]
42. Bhattacharya, R.; Pramanik, P. Semiconductor Liquid Junction Solar Cell Based on Chemically Deposited Bi<sub>2</sub>S<sub>3</sub> Thin Film and Some Semiconducting Properties of Bismuth Chalcogenides. *J. Electrochem. Soc.* **1982**, *129*, 332–335. [[CrossRef](#)]
43. Huang, J.F.; Wang, Y.; Cao, L.Y.; Zhu, H.; Zeng, X.R. Effects of pH Value on the Structures and Optical Properties of Bi<sub>2</sub>S<sub>3</sub> Thin Films. *Key Eng. Mater.* **2010**, *434–435*, 397–399. [[CrossRef](#)]

44. Desai, J.D.; Lokhande, C.D. Nonaqueous chemical bath deposition of Bi<sub>2</sub>S<sub>3</sub> thin films. *Mater. Chem. Phys.* **1993**, *34*, 313–316. [[CrossRef](#)]
45. Yu, Y.; Sun, W.-T. Uniform Bi<sub>2</sub>S<sub>3</sub> nanowires: Structure, growth, and field-effect transistors. *Mater. Lett.* **2009**, *63*, 1917–1920. [[CrossRef](#)]
46. Chao, J.; Xing, S.; Liu, Z.; Zhang, X.; Zhao, Y.; Zhao, L.; Fan, Q. Large-scale synthesis of Bi<sub>2</sub>S<sub>3</sub> nanorods and nanoflowers for flexible near-infrared laser detectors and visible light photodetectors. *Mater. Res. Bull.* **2018**, *98*, 194–199. [[CrossRef](#)]
47. Li, Y.; Zhang, Y.; Lei, Y.; Li, P.; Jia, H.; Hou, H.; Zheng, Z. In situ fabrication of Bi<sub>2</sub>S<sub>3</sub> nanocrystal film for photovoltaic devices. *Mater. Sci. Eng. B* **2012**, *177*, 1764–1768. [[CrossRef](#)]
48. Liu, W.; Guo, C.F.; Yao, M.; Lan, Y.; Zhang, H.; Zhang, Q.; Chen, S.; Opeil, C.P.; Ren, Z. Bi<sub>2</sub>S<sub>3</sub> nanonetwork as precursor for improved thermoelectric performance. *Nano Energy* **2014**, *4*, 113–122. [[CrossRef](#)]
49. Konstantatos, G.; Levina, L.; Tang, J.; Sargent, E.H. Sensitive solution-processed Bi<sub>2</sub>S<sub>3</sub> nanocrystalline photodetectors. *Nano Lett.* **2008**, *8*, 4002–4006. [[CrossRef](#)]
50. He, D.; Wang, Y.; Song, S.; Liu, S.; Luo, Y.; Deng, Y. Polymer-based nanocomposites employing Bi<sub>2</sub>S<sub>3</sub>@SiO<sub>2</sub> nanorods for high dielectric performance: Understanding the role of interfacial polarization in semiconductor-insulator core-shell nanostructure. *Compos. Sci. Technol.* **2017**, *151*, 25–33. [[CrossRef](#)]
51. Ding, Y.H.; Zhang, X.L.; Zhang, N.; Zhang, J.Y.; Zhang, R.; Liu, Y.F.; Fang, Y.Z. A visible-light driven Bi<sub>2</sub>S<sub>3</sub>@ZIF-8 core-shell heterostructure and synergistic photocatalysis mechanism. *Dalton Trans.* **2018**, *47*, 684–692. [[CrossRef](#)]
52. Errando-Herranz, C.; Takabayashi, A.Y.; Edinger, P.; Sattari, H.; Gylfason, K.B.; Quack, N. MEMS for Photonic Integrated Circuits. *IEEE J. Sel. Top. Quantum Electron.* **2020**, *26*, 1–16. [[CrossRef](#)]
53. Xie, Y.-Y.; Ni, P.-N.; Wang, Q.-H.; Kan, Q.; Briere, G.; Chen, P.-P.; Zhao, Z.-Z.; Delga, A.; Ren, H.-R.; Chen, H.-D.; et al. Metasurface-integrated vertical cavity surface-emitting lasers for programmable directional lasing emissions. *Nat. Nanotechnol.* **2020**, *15*, 125–130. [[CrossRef](#)] [[PubMed](#)]
54. Rife, J.C.; Miller, M.M.; Sheehan, P.E.; Tamanaha, C.R.; Tondra, M.; Whitman, L.J. Design and performance of GMR sensors for the detection of magnetic microbeads in biosensors. *Sens. Actuators A Phys.* **2003**, *107*, 209–218. [[CrossRef](#)]
55. Monteiro, O.C.; Trindade, T.; Park, J.-H.; O'Brien, P. The LP-MOCVD of CdS/Bi<sub>2</sub>S<sub>3</sub> bilayers using single-molecule precursors. *Mater. Lett.* **2004**, *58*, 119–122. [[CrossRef](#)]
56. Tian, Y.; Zhang, S.; Tan, W. Oxygen-doping to Bi<sub>2</sub>S<sub>3</sub> thin film and its substrate-dependent resistive switching. *Mater. Res. Express* **2019**, *6*, 116324. [[CrossRef](#)]
57. Jin, J.; He, T. Facile synthesis of Bi<sub>2</sub>S<sub>3</sub> nanoribbons for photocatalytic reduction of CO<sub>2</sub> into CH<sub>3</sub>OH. *Appl. Surf. Sci.* **2017**, *394*, 364–370. [[CrossRef](#)]
58. Ma, J.; Yang, J.; Jiao, L.; Wang, T.; Lian, J.; Duan, X.; Zheng, W. Bi<sub>2</sub>S<sub>3</sub> nanomaterials: Morphology manipulation and related properties. *Dalton Trans.* **2011**, *40*, 10100–10108. [[CrossRef](#)]
59. Dong, Y.; Hu, M.; Zhang, Z.; Zapien, J.A.; Wang, X.; Lee, J.-M. Hierarchical self-assembled Bi<sub>2</sub>S<sub>3</sub> hollow nanotubes coated with sulfur-doped amorphous carbon as advanced anode materials for lithium ion batteries. *Nanoscale* **2018**, *10*, 13343–13350. [[CrossRef](#)]
60. Tian, Y.; Guo, C.F.; Guo, Y.; Wang, Q.; Liu, Q. BiOCl nanowire with hierarchical structure and its Raman features. *Appl. Surf. Sci.* **2012**, *258*, 1949–1954. [[CrossRef](#)]
61. Saitou, M.; Yamaguchi, R.; Oshikawa, W. Novel process for electrodeposition of Bi<sub>2</sub>S<sub>3</sub> thin films. *Mater. Chem. Phys.* **2002**, *73*, 306–309. [[CrossRef](#)]
62. Mane, R.; Sankapal, B.; Lokhande, C. A chemical method for the deposition of Bi<sub>2</sub>S<sub>3</sub> thin films from a non-aqueous bath. *Thin Solid Film.* **2000**, *359*, 136–140. [[CrossRef](#)]
63. Chai, W.; Yang, F.; Yin, W.; You, S.; Wang, K.; Ye, W.; Rui, Y.; Tang, B. Bi<sub>2</sub>S<sub>3</sub>/C nanorods as efficient anode materials for lithium-ion batteries. *Dalton Trans.* **2019**, *48*, 1906–1914. [[CrossRef](#)] [[PubMed](#)]
64. Zhao, G.-Q.; Zheng, Y.-J.; He, Z.-G.; Lu, Z.-X.; Wang, L.; Li, C.-F.; Jiao, F.-P.; Deng, C.-Y. Synthesis of Bi<sub>2</sub>S<sub>3</sub> microsphere and its efficient photocatalytic activity under visible-light irradiation. *Trans. Nonferrous Met. Soc. China* **2018**, *28*, 2002–2010. [[CrossRef](#)]
65. Chen, J.; Qin, S.; Song, G.; Xiang, T.; Xin, F.; Yin, X. Shape-controlled solvothermal synthesis of Bi<sub>2</sub>S<sub>3</sub> for photocatalytic reduction of CO<sub>2</sub> to methyl formate in methanol. *Dalton Trans.* **2013**, *42*, 15133–15138. [[CrossRef](#)] [[PubMed](#)]
66. Liu, S.; Cai, Z.; Zhou, J.; Pan, A.; Liang, S. Chrysanthemum-like Bi<sub>2</sub>S<sub>3</sub> nanostructures: A promising anode material for lithium-ion batteries and sodium-ion batteries. *J. Alloys Compd.* **2017**, *715*, 432–437. [[CrossRef](#)]
67. Yan, X.; Gu, Y.; Li, C.; Zheng, B.; Li, Y.; Zhang, T.; Zhang, Z.; Yang, M. Morphology-controlled synthesis of Bi<sub>2</sub>S<sub>3</sub> nanorods-reduced graphene oxide composites with high-performance for electrochemical detection of dopamine. *Sens. Actuators B Chem.* **2018**, *257*, 936–943. [[CrossRef](#)]
68. Luo, Y.; Chen, H.; Li, X.; Gong, Z.; Wang, X.; Peng, X.; He, M.; Sheng, Z. Wet chemical synthesis of Bi<sub>2</sub>S<sub>3</sub> nanorods for efficient photocatalysis. *Mater. Lett.* **2013**, *105*, 12–15. [[CrossRef](#)]
69. Song, H.; Zhan, X.; Li, D.; Zhou, Y.; Yang, B.; Zeng, K.; Zhong, J.; Miao, X.; Tang, J. Rapid thermal evaporation of Bi<sub>2</sub>S<sub>3</sub> layer for thin film photovoltaics. *Sol. Energy Mater. Sol. Cells* **2016**, *146*, 1–7. [[CrossRef](#)]
70. Li, L.; Liu, Y.; Dai, J.Y.; Zhu, H.X.; Hong, A.J.; Zhou, X.H.; Ren, Z.F.; Liu, J.M. Thermoelectric property studies on Cu<sub>x</sub>Bi<sub>2</sub>Se<sub>2</sub> with nano-scale precipitates Bi<sub>2</sub>S<sub>3</sub>. *Nano Energy* **2015**, *12*, 447–456. [[CrossRef](#)]

71. Ke, J.; Liu, J.; Sun, H.; Zhang, H.; Duan, X.; Liang, P.; Li, X.; Tade, M.O.; Liu, S.; Wang, S. Facile assembly of Bi<sub>2</sub>O<sub>3</sub>/Bi<sub>2</sub>S<sub>3</sub>/MoS<sub>2</sub> n-p heterojunction with layered n-Bi<sub>2</sub>O<sub>3</sub> and p-MoS<sub>2</sub> for enhanced photocatalytic water oxidation and pollutant degradation. *Appl. Catal. B Environ.* **2017**, *200*, 47–55. [[CrossRef](#)]
72. Wang, Q.; Liu, Z.; Feng, H.; Jin, R.; Zhang, S.; Gao, S. Engineering Bi<sub>2</sub>S<sub>3</sub>/BiOI p-n heterojunction to sensitize TiO<sub>2</sub> nanotube arrays photoelectrodes for highly efficient solar cells and photocatalysts. *Ceram. Int.* **2019**, *45*, 3995–4002. [[CrossRef](#)]
73. Adhikari, S.; Kim, D.-H. Synthesis of Bi<sub>2</sub>S<sub>3</sub>/Bi<sub>2</sub>WO<sub>6</sub> hierarchical microstructures for enhanced visible light driven photocatalytic degradation and photoelectrochemical sensing of ofloxacin. *Chem. Eng. J.* **2018**, *354*, 692–705. [[CrossRef](#)]
74. Wu, Z.; Chen, L.; Xing, C.; Jiang, D.; Xie, J.; Chen, M. Controlled synthesis of Bi<sub>2</sub>S<sub>3</sub>/ZnS microspheres by an in situ ion-exchange process with enhanced visible light photocatalytic activity. *Dalton Trans.* **2013**, *42*, 12980–12988. [[CrossRef](#)] [[PubMed](#)]
75. Liang, N.; Zai, J.; Xu, M.; Zhu, Q.; Wei, X.; Qian, X. Novel Bi<sub>2</sub>S<sub>3</sub>/Bi<sub>2</sub>O<sub>2</sub>CO<sub>3</sub> heterojunction photocatalysts with enhanced visible light responsive activity and wastewater treatment. *J. Mater. Chem. A* **2014**, *2*, 4208–4216. [[CrossRef](#)]
76. Zeng, Q.; Bai, J.; Li, J.; Li, Y.; Li, X.; Zhou, B. Combined nanostructured Bi<sub>2</sub>S<sub>3</sub>/TNA photoanode and Pt/SiPVC photocathode for efficient self-biasing photoelectrochemical hydrogen and electricity generation. *Nano Energy* **2014**, *9*, 152–160. [[CrossRef](#)]
77. Zhang, J.; Guo, C.; Tian, Y.; Liu, Q. Superstructure transformations from hexagonal to tetragonal microplates and nested two-dimensional nanonetworks. *Chin. Sci. Bull.* **2014**, *59*, 1787–1793. [[CrossRef](#)]
78. Chen, L.; He, J.; Yuan, Q.; Zhang, Y.W.; Wang, F.; Au, C.T.; Yin, S.F. CuS–Bi<sub>2</sub>S<sub>3</sub> hierarchical architectures: Controlled synthesis and enhanced visible-light photocatalytic performance for dye degradation. *RSC Adv.* **2015**, *5*, 33747–33754. [[CrossRef](#)]
79. Zhao, Y.; Chua, K.T.E.; Gan, C.K.; Zhang, J.; Peng, B.; Peng, Z.; Xiong, Q. Phonons in Bi<sub>2</sub>S<sub>3</sub> nanostructures: Raman scattering and first-principles studies. *Phys. Rev. B* **2011**, *84*, 205330. [[CrossRef](#)]
80. Shaban, H.; Nassary, M.; El-Sadek, M.S.A. Transport properties of Bi<sub>2</sub>S<sub>3</sub> single crystals. *Phys. B Condens. Matter* **2008**, *403*, 1655–1659. [[CrossRef](#)]
81. Yang, J.; Liu, G.; Yan, J.; Zhang, X.; Shi, Z.; Qiao, G. Enhanced the thermoelectric properties of n-type Bi<sub>2</sub>S<sub>3</sub> polycrystalline by iodine doping. *J. Alloy. Compd.* **2017**, *728*, 351–356. [[CrossRef](#)]
82. Tian, Y.; Jiang, L.; Zhang, X.; Zhang, G. A trap-limited-current-based model of Meyer–Neldel rule and its connection to persistent photocurrent. *J. Phys. D Appl. Phys.* **2016**, *49*, 405107. [[CrossRef](#)]
83. Liu, Z.; Pei, Y.; Geng, H.; Zhou, J.; Meng, X.; Cai, W.; Liu, W.; Sui, J. Enhanced thermoelectric performance of Bi<sub>2</sub>S<sub>3</sub> by synergistical action of bromine substitution and copper nanoparticles. *Nano Energy* **2015**, *13*, 554–562. [[CrossRef](#)]
84. Kulbashinskii, V.; Kytin, V.; Maslov, N.; Singha, P.; Das, S.; Deb, A.; Banerjee, A. Thermoelectrical properties of Bi<sub>2</sub>Te<sub>3</sub> nanocomposites. *Mater. Today Proc.* **2019**, *8*, 573–581. [[CrossRef](#)]
85. Fang, J.; Chen, F.; Stokes, K.; He, J.; Tang, J.; O’Connor, C.J. Synthesis and Thermoelectric Properties of Bi<sub>2</sub>S<sub>3</sub> Nanobeads. *MRS Online Proc. Libr.* **2011**, *730*, 55. [[CrossRef](#)]
86. Xi, H.; Liu, Q.; Tian, Y.; Wang, Y.; Guo, S.; Chu, M. Ge<sub>2</sub>Sb<sub>1.5</sub>Bi<sub>0.5</sub>Te<sub>5</sub> thin film as inorganic photoresist. *Opt. Mater. Express* **2012**, *2*, 461–468. [[CrossRef](#)]
87. Zhang, J.; Guo, C.; Wang, Y.; Miao, J.; Tian, Y.; Liu, Q. Micro-optical elements fabricated by metal-transparent-metallic-oxides grayscale photomasks. *Appl. Opt.* **2012**, *51*, 6606–6611. [[CrossRef](#)]
88. Yang, X.; Xiang, W.; Zhao, H.; Zhang, X.; Liang, X.; Dai, S.; Chen, F. Third-order nonlinear optical properties of Bi<sub>2</sub>S<sub>3</sub> nanocrystals doped in sodium borosilicate glass studied with Z-scan technique. *Mater. Res. Bull.* **2011**, *46*, 355–360. [[CrossRef](#)]
89. Yu, X.; Cao, C.; Zhu, H. Synthesis and photoluminescence properties of Bi<sub>2</sub>S<sub>3</sub> nanowires via surfactant micelle-template inducing reaction. *Solid State Commun.* **2005**, *134*, 239–243. [[CrossRef](#)]
90. Jariwala, S.; Sun, H.; Adhyaksa, G.W.; Lof, A.; Muscarella, L.; Ehrler, B.; Garnett, E.C.; Ginger, D.S. Local Crystal Misorientation Influences Non-radiative Recombination in Halide Perovskites. *Joule* **2019**, *3*, 3048–3060. [[CrossRef](#)]
91. Tian, Y.; Zhang, J.; Guo, C.F.; Zhang, B.; Liu, Q. Photoconductive probing of the trap distribution in switchable interfaces. *Nanoscale* **2016**, *8*, 915–920. [[CrossRef](#)]
92. Li, H.; Yang, J.; Zhang, J.; Zhou, M. Facile synthesis of hierarchical Bi<sub>2</sub>S<sub>3</sub> nanostructures for photodetector and gas sensor. *RSC Adv.* **2012**, *2*, 6258–6261. [[CrossRef](#)]
93. Li, M.; Wang, J.; Zhang, P.; Deng, Q.; Zhang, J.; Jiang, K.; Hu, Z.; Chu, J. Superior adsorption and photoinduced carriers transfer behaviors of dandelion-shaped Bi<sub>2</sub>S<sub>3</sub>@MoS<sub>2</sub>: Experiments and theory. *Sci. Rep.* **2017**, *7*, 42484. [[CrossRef](#)] [[PubMed](#)]
94. Jamali-Sheini, F.; Cheraghizade, M.; Heshmatynezhad, L. An efficient wide range photodetector fabricated using a bilayer Bi<sub>2</sub>S<sub>3</sub>/SnS heterojunction thin film. *Semicond. Sci. Technol.* **2019**, *34*, 045008. [[CrossRef](#)]
95. Yu, H.; Wang, J.; Wang, T.; Yu, H.; Yang, J.; Liu, G.; Qiao, G.; Yang, Q.; Cheng, X. Scalable colloidal synthesis of uniform Bi<sub>2</sub>S<sub>3</sub> nanorods as sensitive materials for visible-light photodetectors. *CrystEngComm* **2017**, *19*, 727–733. [[CrossRef](#)]
96. Liu, Y.; Chen, P.; Dai, G.; Su, W.; Sun, Y.; Hou, J.; Zhang, N.; Zhao, G.; Fang, Y.; Dai, N. Single Bi<sub>2</sub>S<sub>3</sub>/Bi<sub>2</sub>S<sub>3-x</sub>O<sub>x</sub> nanowire photodetector with broadband response from ultraviolet to near-infrared range. *Phys. E Low-Dimens. Syst. Nanostruct.* **2020**, *120*, 114041. [[CrossRef](#)]
97. Enke, L.; Bingsheng, Z.; Jinsheng, L. *Semiconductor Physics*; Publishing House of Electronics Industry: Beijing, China, 2003.
98. Chao, J.; Li, H.; Xing, S. Selective synthesis of Bi<sub>2</sub>S<sub>3</sub>/BiOCl composites as electrode for high performance photodetector. *Solid State Sci.* **2019**, *98*, 106034. [[CrossRef](#)]
99. Chen, G.; Yu, Y.; Zheng, K.; Ding, T.; Wang, W.; Jiang, Y.; Yang, Q. Fabrication of Ultrathin Bi<sub>2</sub>S<sub>3</sub> Nanosheets for High-Performance, Flexible, Visible–NIR Photodetectors. *Small* **2015**, *11*, 2848–2855. [[CrossRef](#)]

100. Esparza, D.; Zarazúa, I.; López-Luke, T.; Carriles, R.; Castro, A.T.; De la Rosa, E. Photovoltaic Properties of Bi<sub>2</sub>S<sub>3</sub> and CdS Quantum Dot Sensitized TiO<sub>2</sub> Solar Cells. *Electrochim. Acta* **2015**, *180*, 486–492. [[CrossRef](#)]
101. Moreno-García, H.; Nair, M.; Nair, P. All-chemically deposited Bi<sub>2</sub>S<sub>3</sub>/PbS solar cells. *Thin Solid Films* **2011**, *519*, 7364–7368. [[CrossRef](#)]
102. Moreno-García, H.; Nair, M.T.S.; Nair, P.K. Chemically deposited lead sulfide and bismuth sulfide thin films and Bi<sub>2</sub>S<sub>3</sub>/PbS solar cells. *Thin Solid Films* **2011**, *519*, 2287–2295. [[CrossRef](#)]
103. Fang, M.; Jia, H.; He, W.; Lei, Y.; Zhang, L.; Zheng, Z. Construction of flexible photoelectrochemical solar cells based on ordered nanostructural BiOI/Bi<sub>2</sub>S<sub>3</sub> heterojunction films. *Phys. Chem. Chem. Phys.* **2015**, *17*, 13531–13538. [[CrossRef](#)]
104. Salunkhe, D.B.; Dubal, D.P.; Sali, J.V.; Sankapal, B.R. Linker free synthesis of TiO<sub>2</sub>/Bi<sub>2</sub>S<sub>3</sub> heterostructure towards solar cell application: Facile chemical routes. *Mater. Sci. Semicond. Process.* **2015**, *30*, 335–342. [[CrossRef](#)]
105. Han, M.; Jia, J. 3D Bi<sub>2</sub>S<sub>3</sub>/TiO<sub>2</sub> cross-linked heterostructure: An efficient strategy to improve charge transport and separation for high photoelectrochemical performance. *J. Power Sources* **2016**, *329*, 23–30. [[CrossRef](#)]